A 2D Filling and Solidification Benchmark Test: Validating Smoothed Particle Hydrodynamics (SPH) Simulations for Sand Gravity Casting

Mohammad ZARBINI SEYDANI[1], Abdelkader KRIMI[2], Marie BEDEL[3], Sofiane KHELLADI[1], Mohamed EL MANSORI[3]

[1] **Arts et Metiers Institute of Technology CNAM, LIFSE, HESAM University F-75013 Paris, France**

[2] **Department of Civil, Geological and Mining Engineering, Polytechnique Montréal, Montréal, QC H3T 1J4, Canada**

[3] **MSMP Laboratory, EA-7350, Arts et Metiers ParisTech, 2 Cours des Arts et Metiers, 13617 Aix en Provence, France**

Corresponding author: Mohammad.zarbini_seydani@ensam.eu

Abstract

The simulation of the sand gravity casting process is complicated due to its multiscale and multiphysics nature. Although there are many commercial software options available, it remains extremely difficult to accurately predict the filling, solidification, and defects such as oxidation. Smoothed Particle Hydrodynamics (SPH) is a Lagrangian simulation approach that is particularly well-suited for modeling the gravity casting process. To validate the results of the filling, cooling, and solidification stages of the SPH method, it is interesting to introduce and design a 3D universal experimental test case of the gravity casting process that can be modeled in 2D. This universal test case is developed so that the hydrodynamic filling process can be analyzed in 2D while the cooling and solidification processes can be investigated in 1D. After comparing ProCAST, a commercial 3D mesh-based software, with the 2D SPH method, the results highlight the unique advantages of each approach in analyzing filling stages and temperature evolution. The SPH simulations are better at capturing the essential aspects of fluid motion.

Keywords: Numerical simulation, filling morphology, solidification time, SPH, Gravity casting, 3D Printing mold, universal test case

Table of contents

1. Introduction

The process of sand gravity casting is widely used in manufacturing due to its low cost and simplicity compared to other casting processes [1]. This process involves pouring molten metal into a mold using gravity, and it consists of two main stages: filling and solidification [2]. However, the filling stage can present challenges, such as misrun defects if the part is filled too slowly or turbulent flow causing oxidation if filled too quickly [3] [4]. Detecting misruns is straightforward, but quantifying and locating oxides is more challenging [5]. Turbulent flow during the filling step causes a portion of this film to enter the cast metal, leading to the formation of various defects and a reduction in mechanical properties [4] [6]. Because the casting process occurs inside, forecasting, transferring, and recognizing oxidation in an experiment is challenging and costly [7]. Several research studies have been carried out over the last several decades by researchers to numerically simulate and experimentally validate the relationship between gating factors and casting quality [4]. Accurately forecasting and analyzing the behavior of molten metal, including predicting oxidation, requires a combination of numerical modeling and practical investigation [8]. To better understand the filling process, researchers have conducted extensive research in the areas of thermal analysis and occasionally predicting oxidation and free-surface flow [8] [9].

Minaei et al. [10] predicted the flow pattern within the filling stage of the die cavity using numerical simulation and validated it using a water experimental test cast. Liu et al. [11] investigated the numerical simulation of mold filling in low-pressure casting, validated by a water model using a Plexiglass mold. Im et al. [12] examined the casting process of filling and solidification and discovered that residual flow and natural convection had a substantial influence on all flow properties. Kreziak et al. [13] used the two-phase approach in free-surface tracking to simulate low-pressure casting in a permanent mold. Wenming et al. [14] utilized ProCAST software to conduct numerical simulations of the filling and solidification phases of the low-pressure casting process. It should be mentioned that the simulation results were confirmed by the real experiment. Guofa et al. [15] examined the liquid fraction distribution, temperature field, and solidification pattern of aluminum wheel castings using the ViewCast technology to replicate the

solidification stage of the low-pressure die casting (LPDC). For commercial software such as QuikCAST, ProCAST, MAGMASOFT, and others that utilize mesh-based methods for simulations, the accuracy of the results is greatly influenced by the quality of the mesh used. In these cases, it can be challenging to eliminate artificial diffusion (numerical errors) completely.

The meshless technique is a more suitable method for predicting free surfaces and oxidation defects compared to mesh-based methods. The latter encounters several challenges, including a large number of grid cells, long computation time, and a lack of fluid history. Smoothed particle hydrodynamics (SPH) is a Lagrangian method that is appropriate for modeling the filling process and solidification in gravity casting [16] [17]. This method has some unique advantages, such as the ability to model free surface and material interface behavior, as well as to apply complex physics involving solidification and multiphase flow [18] [19] [20]. While a considerable amount of research has focused on modeling casting processes using SPH, there is a lack of studies that accurately simulate multiple aspects such as filling, cooling, solidification, and oxidation prediction, while also validating the results with experimental data.

Ha et al. [16] employed SPH to model the filling process of gravity die-casting in two dimensions and found the results to be consistent with experimental predictions of the filling step. Cao et al. [21] used the SPH method to improve boundary treatment in the foundry-filling step and conducted water analog experiments, which showed reasonable agreement with SPH models. Based on the SPH approach, Niu et al. [19] developed a mathematical model for the temperature field, including latent heat treatment, in solidification using the SPH approach. The simulation results were compared to WinCast software simulation results, and the strengths of the SPH method were identified.

Cleary et al. [20] claimed that the mesh-based approach only has information about the liquid metal at the free surface. Consequently, the oxide prediction becomes very simple, and the free surface flow is easier to predict. Ellingsen et al. [8] investigated the filling of gravity dies, including the formation and transport of oxides, at two filling speeds. They utilized the SPH method, taking into account slip boundary conditions.

The purpose of this article is to present a 3D test case that can be simplified to a 2D simulation by having uniform filling and solidification in the third direction. This test case can be used to compare numerical

results with 3D experimental data, allowing for the appropriate evaluation of SPH code while reducing the computational costs of 3D simulations. Many researchers have previously introduced benchmark experimental test cases to study the filling and solidification of casting processes.

Chandra [22] provided a set of benchmark test cases designed to evaluate models of latent heat release in pure metals and super alloys. These test cases were analyzed using both 2D and 3D finite element codes for illustrative purposes. B. Sirrel et al. [23] developed a benchmark test case for evaluating flow and solidification modeling of Al castings, which showed good macroscopic performance when turbulence was properly considered. Bonollo et al [24]. aimed to demonstrate the feasibility of using low-pressure die casting for producing safety boxes in chemical, petroleum, and offshore industries. This potential was investigated both technically and economically and compared to other conventional aluminum foundry methods [24]. Carozzan et al. [25] utilized a 3D cellular automaton-finite element solidification model to replicate a benchmark experiment on solidification. This model involved a finite element (FE) solution to account for heat and mass transport in the presence of fluid flow, with differentiation of total mass and solute mass, grain structure prediction, and thermodynamic property computation. On the other hand, Bublk et al. [26] aimed to provide new experimental data to validate well-established mathematical models using the lattice Boltzmann method (LBM) for complex mold cavities in casting processes. The benchmark tests demonstrated the algorithm's ability to produce reliable results, particularly in situations where surface tension effects are significant.

This paper is undertaken to design a universal benchmark test case using a 3D printing mold that could be modeled in 2D for fluid flow and thermal analysis to validate numerical simulation. Moreover, we employed the 2D SPH simulation and 3D ProCAST commercial software to simulate different steps of aluminum gravity casting like filling, transportation, cooling, and solidification.

2. Gravity casting experiment

Figure (1) shows the necessary steps for fluid and thermal flow analysis utilizing experimental and numerical (SPH and ProCAST) data, along with the relevant classification.

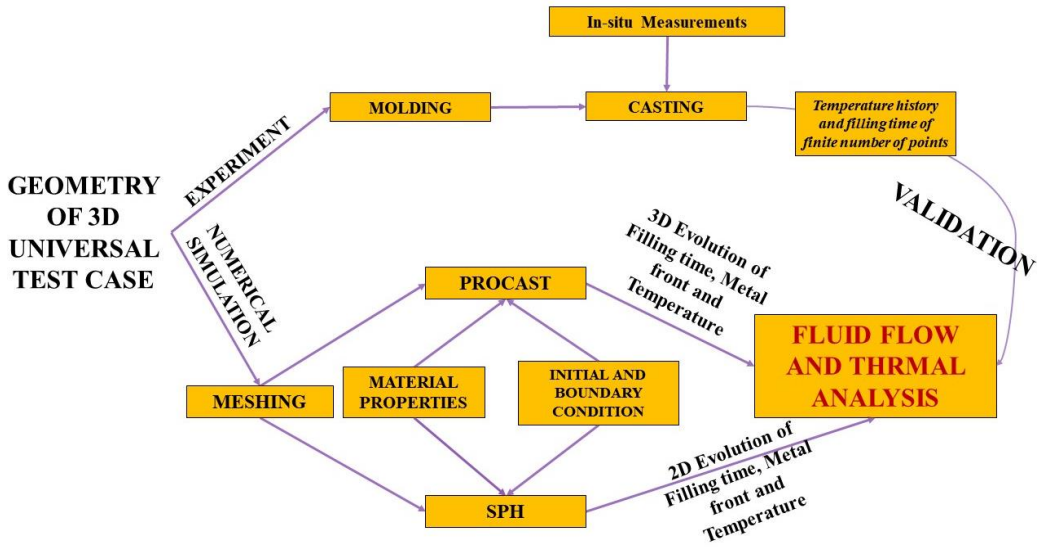

Figure 1 - The required elements for investigating fluid and thermal analysis using experimental and numerical data

2.1. Experimental setup

Figure (2) represents the overall geometry of the proposed experimental test case for gravity casting with a 3D-printed sand mold.

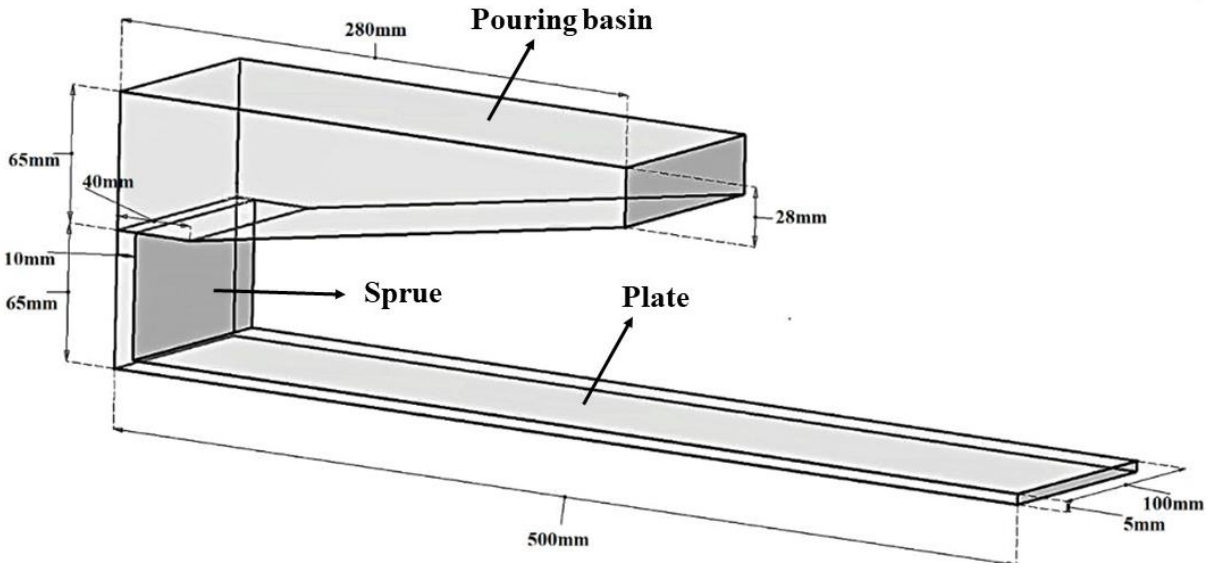

Figure 2 - Schematic of geometry intended for gravity casting

The casting geometry is composed of a pouring basin, a sprue, and a thin plate. In order to model the casting process in two dimensions even if it is not representative of traditional gravity casting geometry,

the whole geometry has a fixed width. The aim is to create a design that enables temperature and velocity variations of the plate to be unaffected by the width direction except in the borders. Therefore, the width and the length of the plate should be deemed enough in comparison with the thickness. As a result, the plate width is 100mm, while the thickness is 5mm. Furthermore, in parallel having a large width size, the length of the test case should be regarded long enough. The pouring basin is filled to a height of 37mm from the bottom in order to completely fill the sprue and plate. The plug is high enough that it can be easily taken out to begin the filling process. Approximately 13mm of molten metal exists at the bottom of the pouring basin after the filling step. Hence, the height of the sprue is considered sufficient (65mm) to prevent the plate from being heated by molten metal left in the pouring basin after the filling phase. Furthermore, the sprue thickness is 10mm to prevent the molten material from solidification inside the sprue when filling. To minimize turbulence and the ingress of sand into the flow, the bottom of the sprue is designed with a crescent-shaped configuration, facilitating a change in the direction of fluid flow. The pouring basin's geometry is such that molten material on the ramp is gradually transported towards the sprue to fill the plate. In addition, it is designed to allow for the use of additional processors to decrease run time when employing the SPH method. In the SPH technique, solid and fluid particles are defined separately. To solve the governing equation, solid and fluid spaces are divided in the direction of x. The design of a "pouring basin" should be taken into consideration in order to have more fluid particles overlap with the solid particles of the plate in the direction of x. As a result, more processors can be used, substantially reducing the simulation time.

A very thin gap is considered at the end of the plate to avoid having to take into account any backpressure induced by air entrapment. To prevent liquid metal from leaking on the measurement connections, an attachment with a proper height is also supplied. It should be mentioned that the molds were printed on an ExOne S-Print Furan machine with a job box size of $800 \times 500 \times 400$ mm^3 [27]. The resin-bonded sand molds composed of a pouring cone, a casting cavity, and a base. It should be mentioned that 3D printed resin-bonded sand molds should have enough resistance to casting and provide gas release permeability.

Casting simulation utilizing commercial software was used to determine the sand mold thickness values surrounding the plate. Figure (3-a) displays the CATIA-designed mold geometry, while Figure (3-b) demonstrates experimental test platform. Both the pouring basin and the top of the sprue are included in the upper component. The upper surface of the plate and the rest of the sprue make up the mold's middle part. Finally, the last component of the mold is the plate underside, which completes the plate shape.

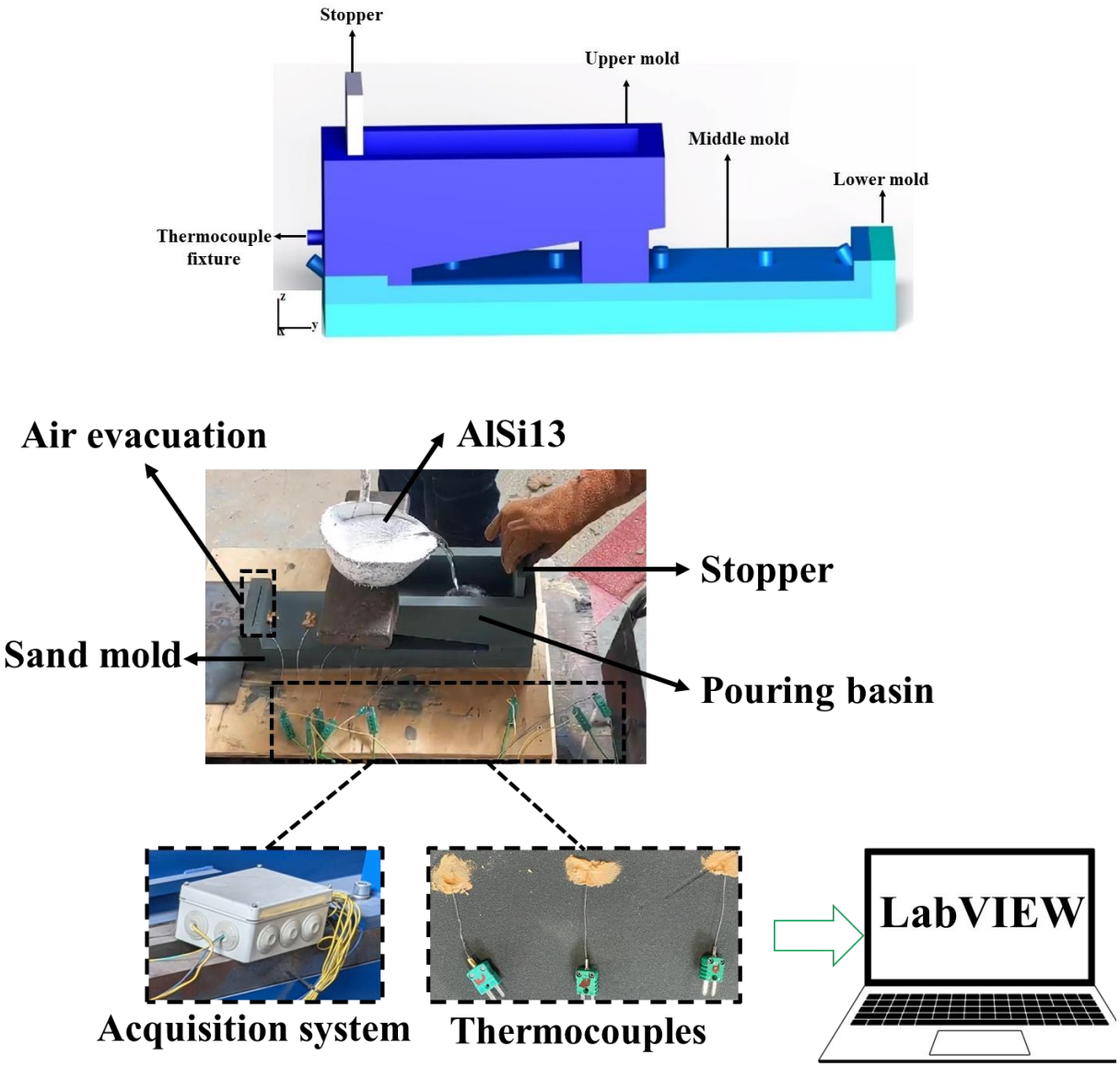

Figure 3 - Geometry of mold a) Top: Designing by CATIA b) Bottom: Experimental test platform

2.2. In situ instrumentation

In a 12Kw resistance furnace (type: NPG.45, voltage: 380V, current: 19A) at 730°C, around 5 kg of AlSi13 (EN AC-4400: US designations of the Aluminum Association) is melted. The temperature of the metal entering the mold differed from that of the furnace, although it was always greater than the liquid temperature. The metal superheat is approximately 130°C, while the pouring temperature is around 700°C. It is worth noting that AlSi13 is slightly hyper eutectic according to the silicon content of 13 wt% (i.e., the eutectic point of the Al-Si is 12.6wt %) [28]. The AlSi13 is commonly utilized in foundry because of fluidity, cast ability, corrosion resistance, and crack resistance [29]. The liquidus and solidus temperatures of AlSi13 in ProCAST commercial software are 572°C and 570°C, respectively, with a temperature difference of only two degrees. As a result, the solidification process occurs at a reasonably constant temperature, making solidification model analysis easier.

An acquisition system and thermocouple positions are placed to measure filling and solidification time at different points in order to examine filling and solidification steps. To characterize the flow dynamics during filling, an acquisition system with an electrical contact is employed to track the fluid in sections. The placement of these bars is intended to monitor filling time from the top of sprue to the end of plate. Steel rods of 1mm diameter are placed with a position precision of 2 mm in the 7 distinct places of the mold, as shown in Figure (4). The circuit is closed when molten metal hits the rods, lowering the resistance and, as a result, decreasing the voltage. The output tension data were collected at a fixed frequency of 100Hz.

K-type thermocouples are inserted at 6 places to characterize temperature evolution in the melt, as shown in Figure (4). The maximum temperature is 700°C in the experiment, hence the thermocouples' precision is $\pm 5.25^{\circ}\mathrm{C}(0.0075 \times |\mathrm{T}'|)$. In parallel, to characterize the flow dynamics during filling, an acquisition system is employed.

The acquisition system was put in nodes (N1, N2, N3, N4, N5, N6, and N7) and thermocouples in nodes (N1 to N8) to capture filling time and temperature, respectively (Figure (4)). N1 is positioned at a distance of 5mm from the top of the sprue. N2 is 2.5mm from the bottom of the plate, at the bottom of the sprue in the central portion of its thickness representing time "t=0s". It should be noticed that the thermocouples N3, N4, N5, and N6 are 100mm, 200mm, 300mm, and 400mm away from the beginning of the plate, respectively. N7 is placed 5mm away from the edge of the plate, precisely at the midpoint of its thickness and width, for the purpose of determining the final filling time. In the width direction, thermocouple N8 is inserted at a distance of 10mm from thermocouple N5. The goal of installing this thermocouple is to compare the temperatures associated with N5 and N8 in order to demonstrate that temperature variations in the center of the plate are independent of changes in the width direction. As a result, the temperature evolution of the 3D experimental test could be described in 2D.

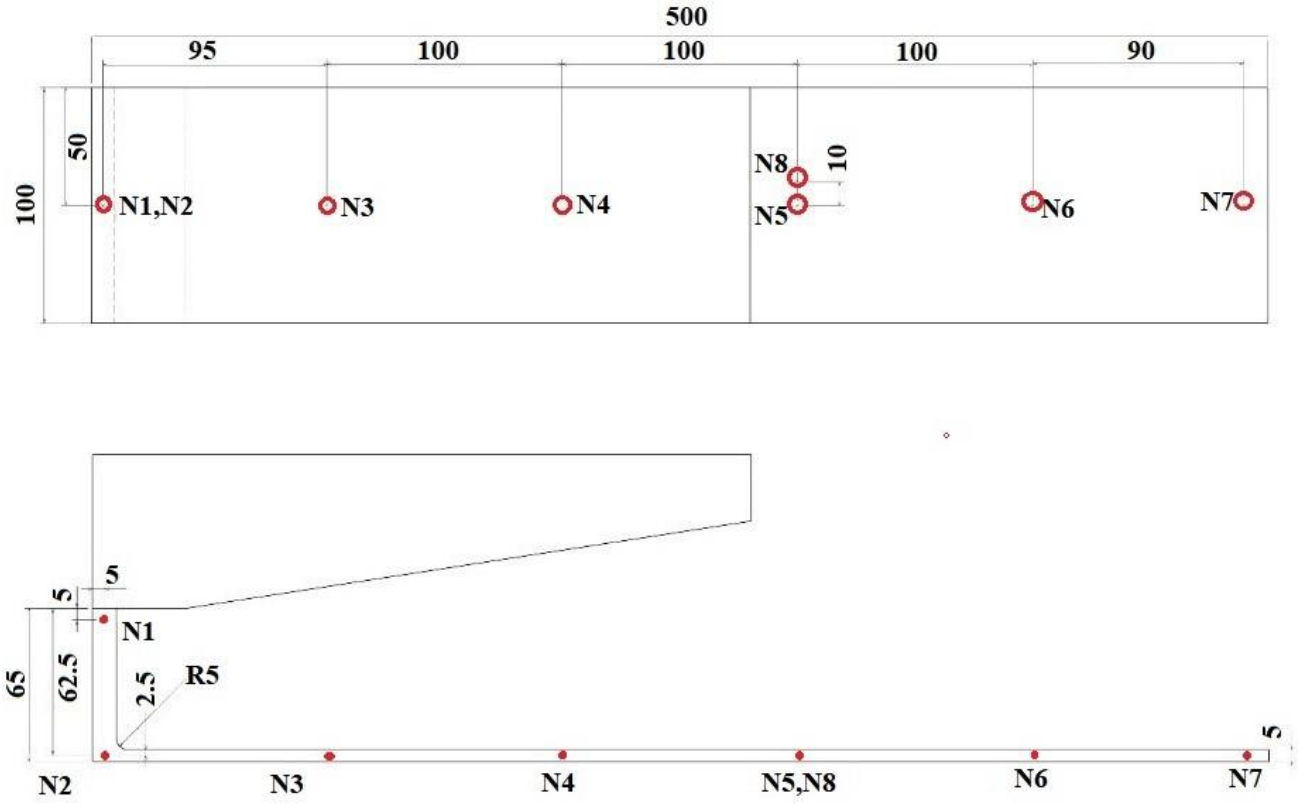

Figure 4 - Location of thermocouples and tracking of molten metal (mm)

2.3 Experimental results

Figure (5) depicts the voltage decrease with time at seven places (N1 to N7). The filling times are 0.09s, 0.13s, 0.13s, 0.15s, and 0.14s between points (N2, N3), (N3, N4) (N4, N5), (N5, N6), and (N6, N7), respectively. Based on the distance between each point in Figure (5), average velocity can be deduced in these locations. The rate of change of velocity is linear with a very good approximation by representing the value 0.9944, as shown in Figure (6), thanks to linear regression and line equation. Given the linear slope obtained from the experimental data, this strongly suggests that the filling velocity is constant. Furthermore, the average velocity is calculated to be 0.7472m/s based on the line's slope. This constant velocity has two significant implications. The fluid is first at a temperature greater than 572°C and its viscosity is constant. Second, the air trapped inside the plate is adequately evacuated and does not slow down the flow of the liquid. It should be mentioned that the Reynolds number in the plate is around 17600, and the flow is therefore turbulent.

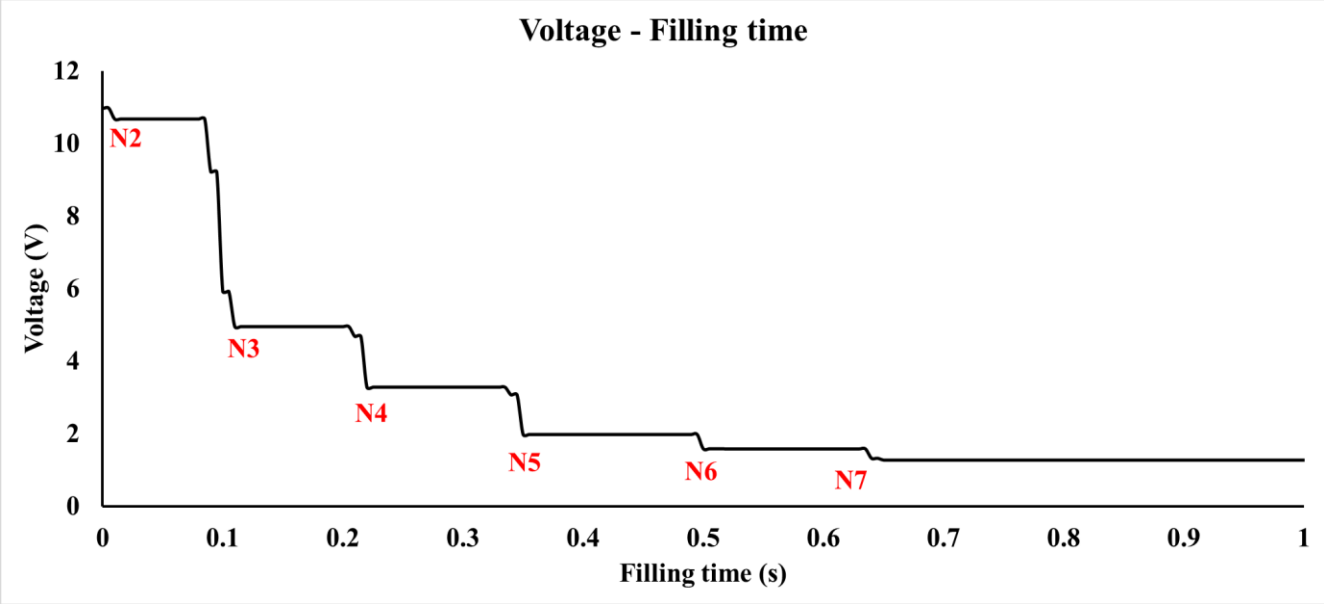

Figure 5 - Voltage versus filling time for different points of experimental test

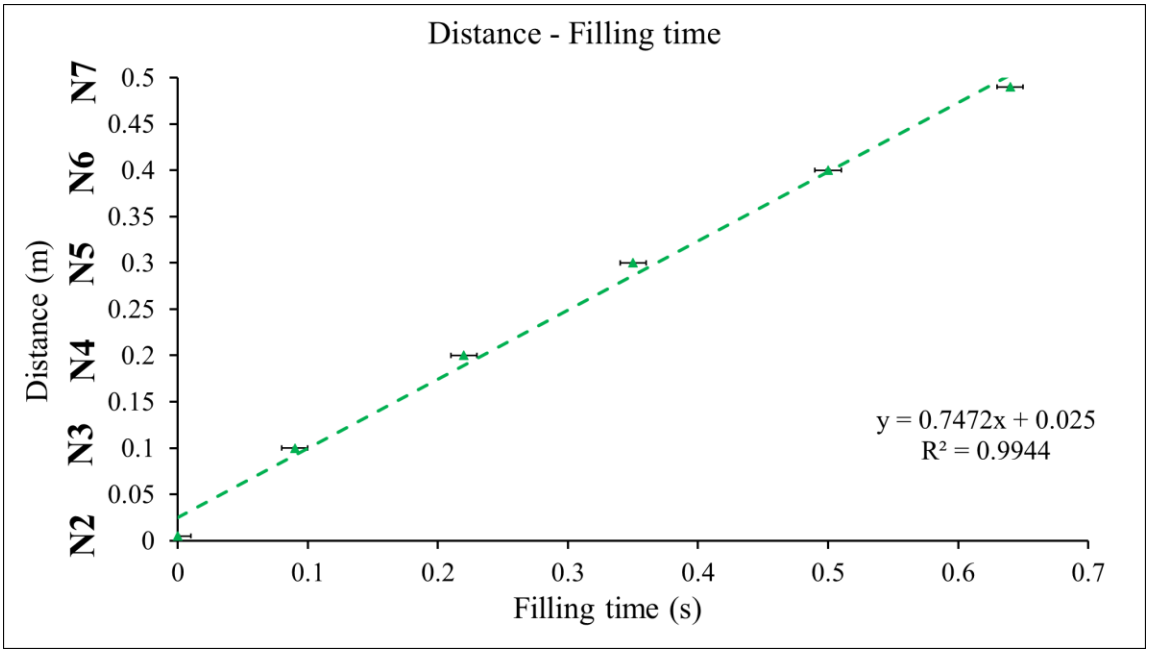

Figure 6 - Distance versus filling time for different points of experimental test

Temperature time curves

Figure (7) depicts the eight temperatures evolution for (N1 to N8). The experimental results revealed temperature heterogeneities in the metal at the end of filling. The cooling curves have three domains. The temperature interval between the pouring temperature and the eutectic nucleation temperature is represented

by the first domain. The alloy is in a liquid form during this zone. A slope of this curve could be used to compute the "cooling rate" of the cast component. The solidification interval of the casting alloy is represented by the second domain. A solidification domain starts with an undercooling process that corresponds with the nucleation of the first eutectic germ and, as a result, the start of alloy solidification. After nucleation, eutectic germs grow, and this process is marked by a plateau of temperature at 570 °C. In eutectic alloys, the plateau duration is a significant correlate of the solidification time. Then in the third domain, the fully solid alloy is cooled until it approaches ambient temperature in the third and final domain. The zero time point in Figure 7 represents the moment when the electrical circuit is closed for the first time. In this experiment, this corresponds to the bottom of the sprue (N2). To clarify further, a reference steel rod is positioned at the top of the sprue (N1), and the circuit is closed when the metal connects N1 to N2.

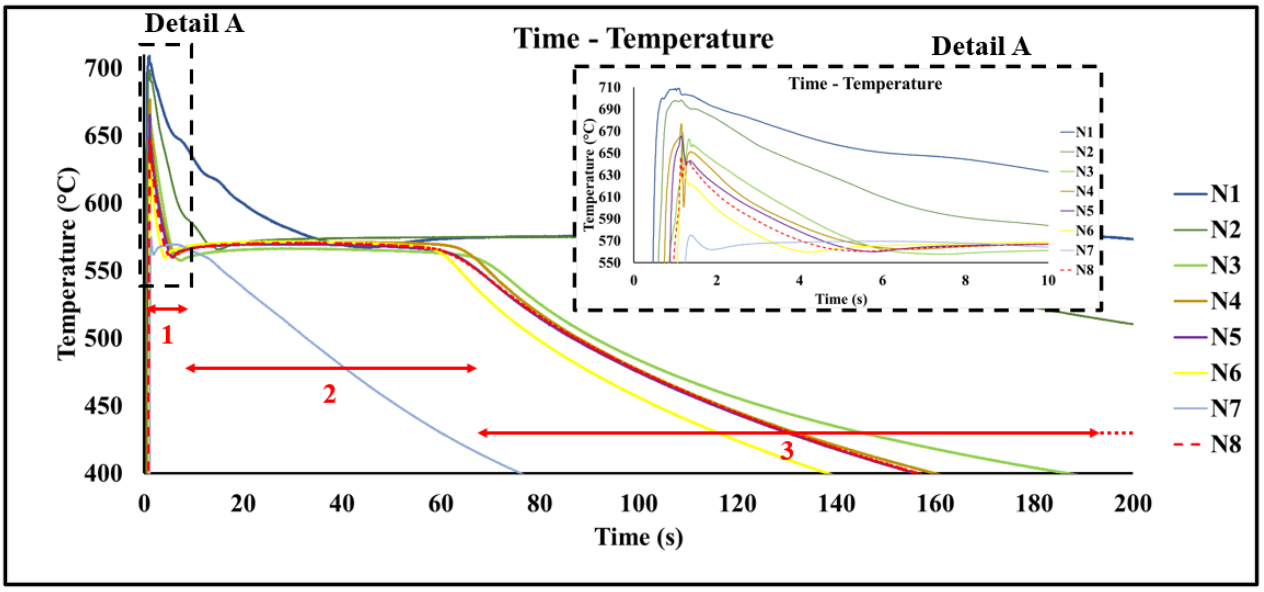

Figure 7 - Experimental cooling curves of AlSi13 alloy for points N1 to N8

N1 at the top of the sprue is used to estimate the initial temperature of casting. The solidification time at various sites is shown in Table (1). The temperature evolution trend for positions N3 through N6, as well as their solidification periods, is remarkably consistent. The cooling rate decreases as the influence of the end-of-plate boundary conditions reduces when we go farther

from the plate's end. Similarly, as we get closer to the plate's end, the solidification time reduces gradually. Furthermore, the highest error percentage between the maximum and minimum solidification times is expected 5.4%. These results indicate that the length of the plate has little effect on the solidification time. The solidification times for locations N5 and N8 are 57s and 56.8s, respectively, with a 0.35% difference. It clearly indicates that the boundary conditions in the direction of the geometry's width have very little impact on the temperature change process, particularly the solidification time, which is negligible. Temperature changes at points N5 and N8 demonstrate that they have the same temperature process. Therefore, the solidification process can be regarded approximately as 1D.

Table 1 – Experimental solidification time for (N3, N4, N5, N6, and N8)

Position of thermocouples	**Cooling rate (Liquid state)** $(\mathrm{T.s^{-1}})$	**Solidification time** (s)	**Cooling rate (solid state)** $(\mathrm{T.s^{-1}})$
N3	**20.37**	**60.83**	**2.29**
N4	**21.08**	**57.5**	**2.52**
N5	**23.84**	**57**	**2.32**
N6	**21.30**	**57**	**2.73**
N8	**23.93**	**56.8**	**2.35**

3. Numerical methodologies

In this article, filling and solidification of sand gravity casting in 2D are modeled using two numerical approaches, the meshless method (SPH) and mesh-based method (commercial software), and the models are then validated through experiments.

3.1 SPH method

3.1.1 Governing equations

The continuity, Navier-Stokes, energy equation, and displacement equation, written in Lagrangian form, for a weakly compressible viscous fluid flow of SPH method are as follows:

$$\begin{cases} \dfrac{D\rho}{Dt} + \rho\nabla.\vec{V} = 0 \\ \rho\dfrac{D\vec{V}}{Dt} = -\nabla P + \rho\vec{g} + F^{Vis} + A(\phi)\vec{V} \\ \dfrac{DH}{Dt} = \nabla.(k\ \nabla T\ ) \\ \dfrac{D\vec{r}}{Dt} = \vec{V} \end{cases} \tag{1}$$

The symbols "$\dfrac{D(.)}{Dt}$" and "∇" correspond to the substantial derivative in Cartesian coordinates and the nabla operator, respectively.

ρ, p, V, r, T, k, H and g represent density, pressure, velocity vector, position vector, temperature, thermal conductivity, enthalpy, and gravitational acceleration vector, respectively. F^{Vis} and $A(\phi)\vec{V}$ demonstrate viscosity force and phase-changing terms to make flow behave like a porous medium using Carman-Kozney equations [30] . The WCSPH technique [31] (weakly compressible smoothed particle hydrodynamics) is employed in this study. In this work, the following equation of state is used to calculate pressure which is shown as:

$$P = P_r(\frac{\rho}{\rho_0} - 1) + P_b \tag{2}$$

Where ρ_0 indicates the reference density, P_r represents the reference pressure and P_b means the background pressure. The reference pressure is a function of the reference density and reference sound speed c_0 for the linear constitutive equation of state provided by equation (3).

$$P_r = \rho_0 c_0^2 \tag{3}$$

According to the stability criteria, using the physical speed of sound as a reference results in a very tiny time step. As a consequence the value of c_0 is found as follows:

$$c_0^2 \geq \max\left\{\frac{U_0^2}{\delta\rho}, \frac{\| g \| L_0}{\delta\rho}, \frac{\mu U_0}{\rho_0 L_0 \delta\rho}\right\} \tag{4}$$

The reference velocity, reference length, and dynamic viscosity, respectively, are U_0, L_0, and μ. $\delta\rho$ denotes the dimensionless density variation, which is set at 1% ($\delta\rho = 0.01$) [32]. The background pressure is usually set to zero $(P_b = 0)$ in order to simulate free surface flow. However, in confined flow scenarios, a positive value is used for this parameter to avoid tensile instability. Based on experimental measurements, the average velocity of molten metal (1 m/s) is utilized to calculate the artificial sound speed. While the incompressible technique was used in ProCAST, the artificial sound speed value is obtained (10 m/s). It should be mentioned that the maximum variation of density $(\delta\rho)$ is around 1%.

3.1.2 Discrete form of governing equation

SPH is a particle-based method for modeling fluid flow, heat transport, and complex physics such as multiphase flow and solidification [33] [34]. SPH is a Lagrangian continuum approach, which means that each particle follows complex flows automatically, unlike standard Eulerian methods [35] [36]. SPH uses interpolation kernels [35] [36] to smooth out particle density, pressure, and other individual properties based on neighboring particles. The interpolated value of a field function A at any location r expresses using the SPH approach [35] [36]:

$$A(r_i) = \sum_{j=1}^{N} \frac{m_j}{\rho_j} A(r_j) W_{ij} \tag{5}$$

This equation represents the sum of all j particles in the support domain (within a radius $2h$ of r) of the i particle. m_j, ρ_j and $W_{ij} = W(r_i - r', h)$ refer to the mass density and the kernel function respectively

[36]. The smoothing length h is a constant determined in relation to the initial inter-particle distance δx_0 $(h = 2\delta x_0)$ in this study [19] [36]. $V_0' = \delta x_0^d$ is the initial particle volume, where d is the space dimension number. The Kernel function satisfies the smoothness, compact support, normalizing requirement, and regularity. [18] [19] [36].

$$W(r,h)_{2D} = \alpha_{2d} \begin{cases} (1-\frac{r}{2h})^4 (2\frac{r}{h}+1) & 0 \le \frac{r}{h} < 2 \\ 0 & else \end{cases} \tag{6}$$

Where α_{2d} is equal to $\frac{7}{4\pi h^2}$. Fluid properties are determined using smoothing gradients. The gradient of the function A is then given by [36]:

$$\nabla A(r_i) = \sum_{j=1}^{N} \frac{m_j}{\rho_j} A(r_j) \nabla W_{ij} \tag{7}$$

Many improvements have been made to the SPH approach in order to model free surface flows with less numerical noise and tensile instability [37] [38]. The $\delta - SPH$ [39] [40] technique was utilized to increase the accuracy and limit the noise of numerical implementation for simulating the isothermal phase change process for Navier-Stokes and energy equations in this study. Weakly compressible and Newtonian assumptions have been applied to continuity, momentum, energy, and equation of state. For additional information, see [41] [42].

Continuity equation: Under the hypotheses that have been explained above, the continuity equation for $\delta - SPH$ a model is like the following [39] :

$$\frac{D\rho_i}{Dt} = -\rho_i \sum_j (V_j - V_i).\nabla_i W_{ij} V_j' + hc_0 \sum_j \delta\, D_{ij}.\nabla_i W_{ij} V_j' \tag{8}$$

The symbol ∇_i represents the gradient taken, which is referred to as the coordinates of the particle i. V_j' presents the volume of $j-th$ particle. The diffusive term which has been shown with D_{ij}.

$$D_{ij} = 2[(\rho_j - \rho_i) - \frac{1}{2}(<\nabla\rho>_j^L + <\nabla\rho>_i^L).(r_j - r_i)]\frac{(r_j - r_i)}{|r_j - r_i|^2} \tag{9}$$

The symbol $<\nabla\rho>_i^L$ indicates the renormalized density gradient that has been defined as [43]:

$$<\nabla\rho>_i^L = \sum_j (\rho_j - \rho_i) L_i \nabla_i W_{ij} V_j' \tag{10}$$

$$L_i = [\sum_j (r_j - r_i) \otimes \nabla_i W_{ij} V_j']^{-1} \tag{11}$$

δ is a crucial parameter that determines the magnitude of density diffusion [39]. The range of this dimensionless parameter is limited and usually sets to 0.1 in $\delta - SPH$. For more details, refer to [41] [42].

Momentum equation: Equation (12) represents momentum equation for $\delta - SPH$ method [41].

$$\frac{DV_i}{Dt} = -\frac{1}{\rho_i}\sum_j (p_i + p_j)\nabla_i W_{ij} V_j' + hc_0 \frac{\rho_0}{\rho_i}\sum_j \alpha\pi_{ij}\nabla_i W_{ij} V_j' + g_i + \frac{A(\phi_s)V_i}{\rho_i} \tag{12}$$

Monaghan and Gingold [44] introduced artificial viscosity to the momentum equation to improve stability.

$$\pi_{ij} = \frac{(V_j - V_i).(r_j - r_i)}{(r_j - r_i)^2} \tag{13}$$

In $\delta - SPH$, the momentum equation incorporates a viscous dissipation term, determined by the dimensionless parameter α which is locally constant, ranges from 0.01 to 0.05 [39]. In this model, the fluid simulates solidification by acting as a porous medium, consisting of three zones: solid, liquid, and mushy. The particles' velocity gradually decreases from a finite value in the liquid zone to zero in the solid state. This technique utilizes a porosity parameter, referred to as the 'liquid fraction' or ϕ, to represent the fluid's

behavior as a porous medium. Brent et al. [45] proposed a linear function for A in the case of an isothermal phase transition.

$$A(\phi) = -C_A(1-\phi) \tag{14}$$

C_A represents a constant parameter that is 10^5 in this investigation. This linear function has the advantage of having a low computing cost. The influence of the porosity function on the momentum equation is explained in three steps in the following:

- In the full liquid region (i.e., when $\phi = 1$), the function A vanishes and then has non-influence on the momentum equation.
- The porosity function has a gradual variation between the liquid and solid sections while in the mushy/regularization region (i.e., when $0 < \phi < 1$).
- In the full solid region (i.e., when $\phi = 0$), the function A will take a tremendous value. As a result, it swamps out all other terms in the momentum equation over the time variation of the velocity. Therefore, the new anticipated velocity is set to zero.

Energy equation: The total enthalpy formulation for conduction in phase-changing materials is summarized as follows [46]:

$$\frac{DH_i}{Dt} = \nabla.(k_i \nabla T_i) \tag{15}$$

In equation (15) k_i and T_i represent the thermal conductivity and temperature for each particle. H_i is total enthalpy and it can be expressed in one equation that regroups all phases as a sum of sensible heat h_s and latent heat h_l following [47].

$$H(T) = h_s + h_L = \int_{T_r}^{T} < C > dT + \rho_l \phi L_h \tag{16}$$

L_h shows latent heat of metal or alloy. T_r represents reference temperature, and the value of it depends on the process type, which is isothermal or non-isothermal. If the phase change process is isothermal (pure material), the amount of it is equal to the melting temperature $(T_r = T_m)$, else if the phase change phenomena are non-isothermal, the value of T_r is obtained from the average of two liquidus and solidus temperatures $(T_r = \frac{T_s + T_l}{2})$.

This symbol $<.>$ defines as follows:

$$<.>= (1-\phi)(.)_s + \phi(.)_l \tag{17}$$

C Indicates volumetric heat capacity, which is presented below:

$$C_i = \rho_i c_p \tag{18}$$

In equation (18), c_p and ρ_i are the specific heat capacity when the pressure is constant and density of each particle, respectively. Volumetric local liquid fraction has been shown by ϕ, and this parameter can be shown as a discontinuous Heaviside step function.

$$\phi(T) = \mathfrak{H}(T - T_r) \tag{19}$$

For isothermal phase change, a volumetric liquid fraction or temperature-dependent function can be used. Using a discontinuous Heaviside step function in numerical simulations leads to non-physical characteristics [46] [48]. A smooth fraction function can solve both isothermal and non-isothermal phase transition issues [49] [50]. The equation now includes the regularized volumetric fraction as a function of temperature.

$$\phi(T) = \begin{cases} 0 & T < T_r - \varepsilon(solid) \\ \frac{1}{2}\{1 + \sin(\pi(\frac{T - T_r}{2\varepsilon}))\} & T_r - \varepsilon \le T \le T_r + \varepsilon(mushy) \\ 1 & T > T_r + \varepsilon(liquid) \end{cases} \tag{20}$$

In equation (20), ε represents a smoothing parameter of a Heaviside step function within a region of 2ε in the case of isothermal phase change. By assuming a constant volumetric capacity C for each phase and applying the chain rule, the derivative of equation (16) with respect to t can be expressed as follows

$$\frac{DH}{Dt} = \left\{ < C > + \rho_l L \frac{d\phi}{dT} \right\} \frac{DT}{Dt} = \tilde{C} \frac{DT}{Dt} \tag{21}$$

C' is equivalent to volumetric heat capacity. Therefore, by using this entire hypothesis, then the enthalpy equation can be rewritten for all phases as:

$$\tilde{C}_i \frac{DT_i}{dt} = \nabla.(< k_i > \nabla T_i) \tag{22}$$

It should be mentioned that the new SPH formulation of the Laplacian operation was introduced by Schwaiger [51]. was used to improve the accuracy near free surface boundaries.

3.1.3 Boundary condition

Fluid boundary condition:

In this work, we also used a multiphase fluid flow adaptation of the generalized wall boundary condition approach suggested by [32] [52]. Three layers of dummy particles must be applied to the wall interface in the normal direction using this approach (see Figure (8)). This approach may be used to create free-slip or no-slip wall boundary conditions. In the computation of fluid viscous forces, the free-slip boundary condition is implemented by ignoring the viscous interaction between the fluid particle and the nearby dummy particles.

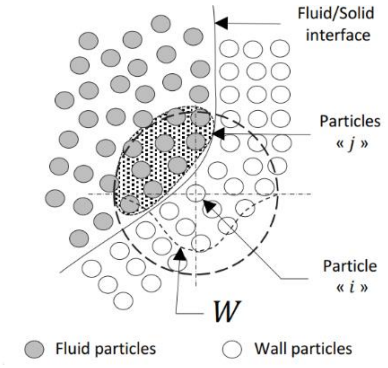

Figure 8 - Geometrical description of different parameters used in the generalized wall Boundary condition [32].

According to [32] [52] , the pressure in the dummy-wall particle is computed from the pressure in the nearby fluid particles j .

$$p_w = \frac{\sum_j^{n_f} p_j W_{ij} + g \sum_j^{n_f} \rho_j r_{wj} W_{wj}}{\sum_j^{n_f} W_{ij}} \tag{23}$$

Thermal boundary condition

The non-homogeneous thermal Neumann boundary condition $\nabla T.n = q$ is developed in this work. The following equation is developed in this work to represent thermal Neumann boundary conditions on the material particles (liquid, mushy/regularization, and solid regions) by the relevant wall particles.

$$T_{wall_i} = \frac{q \sum_j^{n_b} r_{ij} \frac{\partial W}{\partial r} V_j' + d \sum_j^{n_b} T_j V_j' \nabla W.n_i}{d \sum_j^{n_b} V' \nabla W.n_i} \tag{24}$$

Here q represents a heat flux ($q = 0$ for the adiabatic conditions) and n_i is the normal vector to the wall.

3.2 ProCAST Simulation

ProCAST is commercial software using the finite element method to model the whole casting process from filling through solidification. A three-dimensional thermal-hydraulic simulation of AlSi13 alloy gravity casting in the resin-bonded sand mold is performed through ProCAST [53] [54]. The liquid alloy of AlSi13 is an incompressible Newton fluid [55]. The whole 3D continuity and Navier-Stokes equations were solved as well as heat conservation to model filling and solidification of gravity casting process [53] [54].

Continuity equation: $$\nabla.\vec{V} = 0 \tag{25}$$

Navier Stokes (Momentum equation): $$\rho \frac{D\vec{V}}{Dt} = \rho\vec{g} - \nabla p + \nabla.(\mu\nabla\overrightarrow{V}) \tag{26}$$

Energy equation: $$\rho c_p \frac{DT}{Dt} = \nabla.(k\nabla T) + \rho L \frac{\partial \phi_s}{\partial t} \tag{27}$$

Solidification Path: $$\phi_s = (\frac{T - T_l}{T_l - T_s}) \tag{28}$$

In ProCAST simulation, solidification is assumed to follow a linear path. The minimum time step is 0.01s, while the maximum time steps for filling and solidification are 0.1s and 1s, respectively. Thermal properties of resin-bonded sand and AlSi13 alloy are provided in Table (2) of the ProCAST database. The latent heat value of AlSi13 is $522kJ/kg$. The liquidus and solidus temperatures in the database are 572°C and 570°C, respectively. The density of resin-bonded sand is assumed constant. As the molten metal enters the mushy area below 570 degrees and at less than 100 kg.m/s, the viscosity of AlSi13 increases. This prioritizes the viscosity term and stops fluid movement to simulate the solidification process

Table 2 - Thermal properties of the resin-bonded sand and the AlSi13 alloy in ProCAST database

Temperature (°C)	Density ($kg.m^{-3}$)	Specific heat ($J.kg^{-1}.K^{-1}$)	Conductivity ($W.m^{-1}.K^{-1}$)	Viscosity ($kg.m^{-1}.s^{-1}$)
Resin-bonded sand properties				
20		670	0.71	
100		800	0.68	
200		920	0.64	
300		883	0.60	
400	1590	1006	0.56	
500		1006	0.53	

600		1006	0.50	
700		1006	0.60	
900		1006	0.73	
AlSi13 alloy properties				
300	2600	1020	151.6	100
450	2578	1130	147	100
550	2563	1200	144	100
570	2560	1210	143.5	100
572	2478	1210	80	0.001
750	2431	1210	80	0.001

3.3 Comparison between SPH and ProCAST

The fundamental distinction between the two approaches is that the SPH method is Lagrangian, whereas the commercial ProCAST software is Eulerian. The SPH approach is a meshless method, whereas the ProCAST computation is mesh-based. Contrary to ProCAST, the SPH approach is able to get the temporal history of material particles. Free surfaces, material interfaces, and changing boundaries can all be tracked automatically in the SPH, regardless of particle movement complicity. The main equations of the WCSPH and ProCAST models, as well as the differences between them, are shown in Table (3).

Table 3 - Comparison of ProCAST and WCSPH model

WCSPH		**ProCAST software**
Weakly compressible flow		**Incompressible flow**
$\frac{\partial \rho}{\partial t} + \rho \nabla . \vec{V} = 0$	**Continuity equation**	$\nabla . \vec{V} = 0$
$\rho \frac{D\vec{V}}{Dt} = \rho \vec{g} - \nabla p + \nabla . (\mu \nabla \vec{V}) + A(\phi)$	**Momentum equation**	$\rho \frac{D\vec{V}}{Dt} = \rho \vec{g} - \nabla p + \nabla . (\mu \nabla \vec{V})$
$\tilde{C} \frac{DT}{Dt} = \nabla . (k \nabla T)$ $\tilde{C} = (1 - \phi)\rho_s C_s + \phi \rho_l C_l + \rho_l L_f \frac{d\phi}{dT}$	**Energy equation**	$\rho C_p \frac{DT}{Dt} = \nabla . (k \nabla T) + \rho L \frac{\partial \phi_s}{\partial t}$
$\phi(T) = \begin{cases} 0 \\ \frac{1}{2}\{1 + \sin(\pi(\frac{T - T_r}{2\varepsilon}))\} \\ 1 \end{cases} \rightarrow \begin{bmatrix} T < T_r - \varepsilon(solid) \\ T_r - \varepsilon \leq T \leq T_r + \varepsilon(mushy) \\ T > T_r + \varepsilon(liquid) \end{bmatrix}$	**Solid fraction**	$\phi_s = \left(\frac{T - T_s}{T_l - T_s}\right)$

The SPH technique presents challenges in calculating pressure for incompressible flow, leading to the adoption of weakly compressible SPH (WCSPH). WCSPH allows for pressure calculation using the equation of

state. Regarding solidification modeling in fluid flow, the ProCAST method utilizes the viscosity increase model, while the SPH method employs the Carman-Kozeny equation to incorporate solidification into the momentum equation. The Carman-Kozeny equation introduces an additional source term in the momentum equation that effectively hinders fluid flow during the mushy area. In terms of the energy equation, the WCSPH approach embeds latent heat within the heat capacity, while ProCAST software treats latent heat as a separate source term. WCSPH employs equal heat capacity, which includes latent heat in the energy equation. On the other hand, ProCAST assumes a linear relationship for solid fractions, while the WCSPH technique uses a sine function. It's important to note that ProCAST simulation is based on the QuikCAST data set, as mentioned before. The SPH approach defines thermal conductivity in the same manner as the ProCAST simulation. The QuikCAST dataset was used to determine the maximum and minimum values for density and heat capacity, which were then computed using equation (17).

3.4 Initial and boundary conditions

3.4.1 Initial condition

Hydraulic: It should be highlighted that the fluid is initially motionless, as in the experiment done, while applying the initial and boundary conditions relevant to fluid dynamics. The fluid begins to flow as a natural consequence of gravity.

Thermal: The thermocouple (N1) is placed at the top of the sprue. The maximum temperature, relying on this, is roughly 700 °C, which is used as an initial condition for numerical simulation. The mold wall's initial temperature is about 20 °C, which is the same as the ambient temperature.

3.4.2 Boundary condition

Hydraulic: The WSHEAR (wall shear) method is used to account for a velocity boundary layer along the mold wall in ProCAST simulation. The value of WALLF is set to 0.99, which correlates to more wall slips. In addition, Perfect slip is defined as the boundary condition between the wall and the fluid in SPH method. Furthermore, the symmetric boundary condition for walls in the direction perpendicular to the transverse axis is used in ProCAST simulation.

Thermal: In order to model cooling and solidification, the Neumann boundary condition (Conduction) is employed in both WCSPH and ProCAST simulations to estimate heat extraction at metal/mold interface. The heat flux exiting the mold surface is supposed to be constant by three levels as illustrated in Table (4) and Figure (9). The cooling of molten metal above liquidus temperature, the solidification process between liquidus and solidus temperature, and the cooling of solids at temperatures below solidus temperature are the three zones covered. The values are calculated based on experimental data using one-dimensional calculations in such a way those three zones (liquid metal cooling, phase transition, and solid metal cooling) were considered. The way for calculating the value of q using one-dimensional equations is shown below. It should be mentioned that T_0, T_L, T_S, and T_{end} represent initial, liquidus, solidus, and temperature at 100s. In addition, the average experimental periods $(t_{\exp})$ between corresponding temperatures in each location (N3 to N7) were utilized to derive these values.

Table 4 - One-dimensional equation to obtain Neumann boundary conditions in three different zones

Zone (1)	$\mathrm{q} = -\mathrm{K}\frac{\partial \mathrm{T}}{\partial \mathrm{x}} = \frac{\rho \mathrm{e} \mathrm{C_p}(\mathrm{T_0} - \mathrm{T_L})}{\mathrm{t_{exp}}} \approx 133000 \frac{\mathrm{W}}{\mathrm{m}^2}$
Zone (2)	$\mathrm{q} = -\mathrm{K}\frac{\partial \mathrm{T}}{\partial \mathrm{x}} = \frac{\rho \mathrm{e} \mathrm{L} + \rho \mathrm{e} \mathrm{C_p}(\mathrm{T_L} - \mathrm{T_S})}{\mathrm{t_{(exp)}}} \approx 61000 \frac{\mathrm{W}}{\mathrm{m}^2}$
Zone (3)	$\mathrm{q} = -\mathrm{K}\frac{\partial \mathrm{T}}{\partial \mathrm{x}} = \frac{\rho \mathrm{e} \mathrm{C_p}(\mathrm{T_S} - \mathrm{T_{end}})}{\mathrm{t_{(exp)}}} \approx 19000 \frac{\mathrm{W}}{\mathrm{m}^2}$

In the first period, when the mold is still cold and the metal is liquid, the heat extraction is high owing to the thermal gradient between the mold and the molten material, q is equal to $(133000 \frac{\mathrm{W}}{\mathrm{m}^2})$. The value of q then reduces to the value of $(61000 \frac{\mathrm{W}}{\mathrm{m}^2})$ in the second stage, and to $(19000 \frac{\mathrm{W}}{\mathrm{m}^2})$ in the third or final stage.

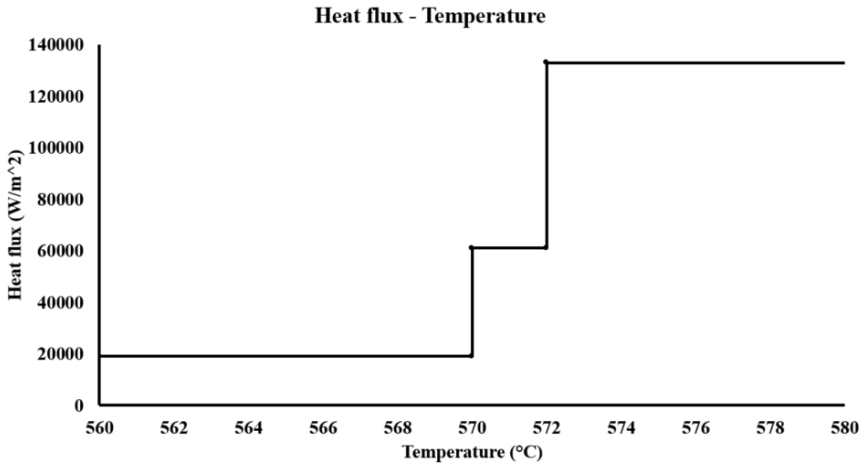

Figure 9 - q values of Neumann boundary condition versus temperature for WCSPH method

The ProCAST program has a limitation on the use of Neumann thermal boundary conditions. The Neumann boundary condition cannot be imposed as a function of temperature; therefore, in this software, it must be defined as a function of time. Because of this problem, it will be problematic if the casting geometry has different thicknesses. By applying this boundary condition, for example, Part A's solidification time could differ from Part B's, thus when the boundary condition is adjusted at a certain point in time, Part A could still be in the liquid cooling zone while Part B has into the solidification zone. The curves in one zone can subsequently have two different slopes, which is inappropriate. The average time of each zone is also calculated for ProCAST simulation in order to apply the Neumann boundary condition there.

3.5 Mesh and convergence

CAD models of the part, gating system, and sand mold are created in CATIA V5 software and imported into ProCAST. Linear tetrahedral elements with a 1.5mm mesh size are used for both the part and mold. To ensure mesh independence, several refinement trials are conducted to determine the appropriate mesh size. Figure (10) shows the trend of mesh independence during the casting process. Results from filling simulations using different cell numbers in ProCAST remain consistent, indicating mesh independence. With larger cell sizes, ProCAST predicts lower velocity values, which converge as the cell size decreases. On the other hand, the SPH approach exhibits the opposite trend, with overestimated velocity values that converge as the number of particles increases. Based on these findings, a cell count of 529133 (corresponding

to a 1.5mm size) is chosen for the ProCAST simulation. Similarly, for the SPH technique, the results become independent of the number of particles when the count exceeds 10491 (corresponding to a 1mm distance between particles).

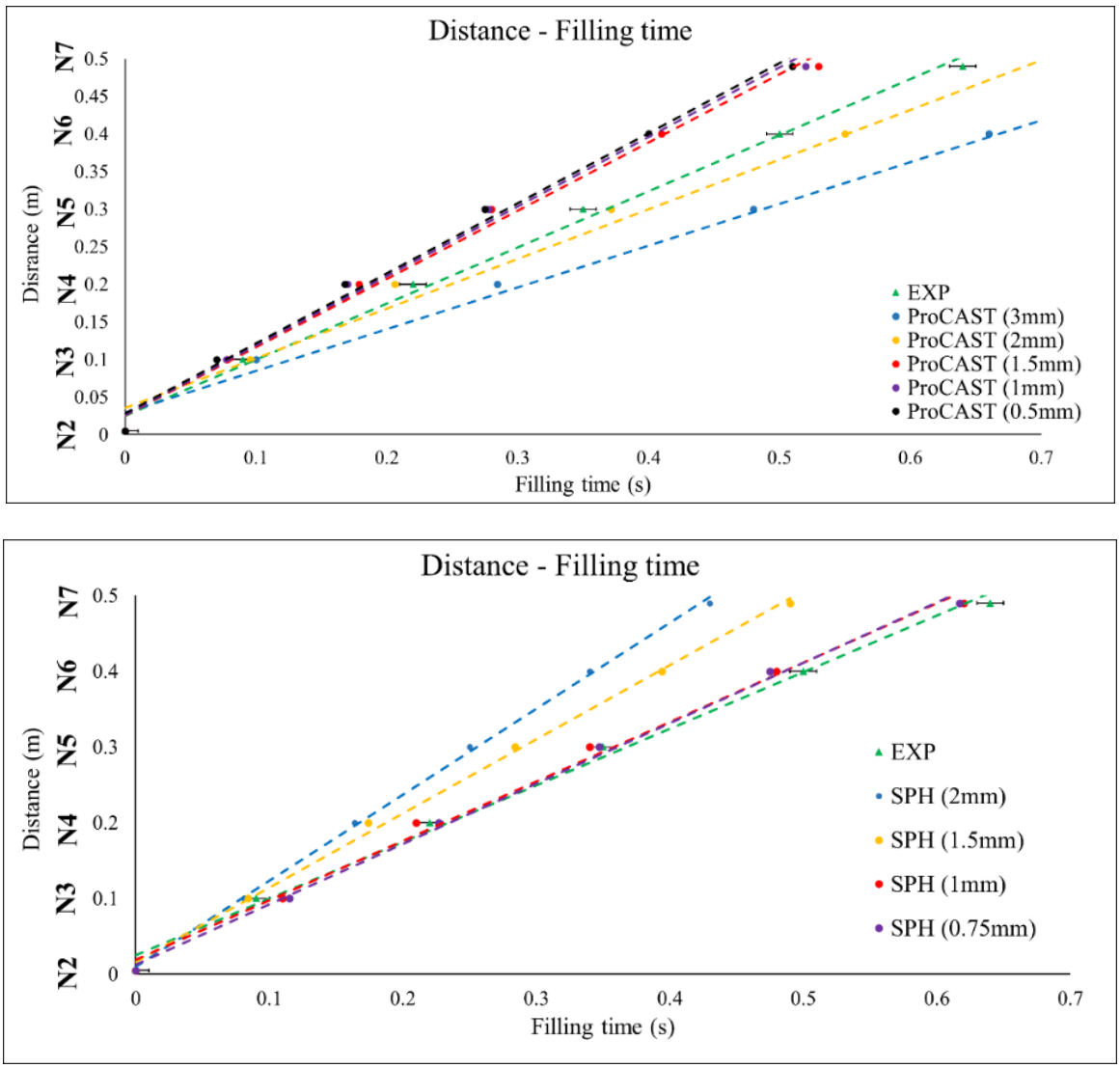

Figure 10 - Mesh independency of filling step for ProCAST and SPH simulation

Figures (11) and (12) illustrate the schematic mesh in ProCAST and the particle distribution using the 2D SPH approach. It should be noted that the calculation time for the 2D SPH method and 3D ProCAST simulation using the appropriate meshes is equivalent to roughly one day.

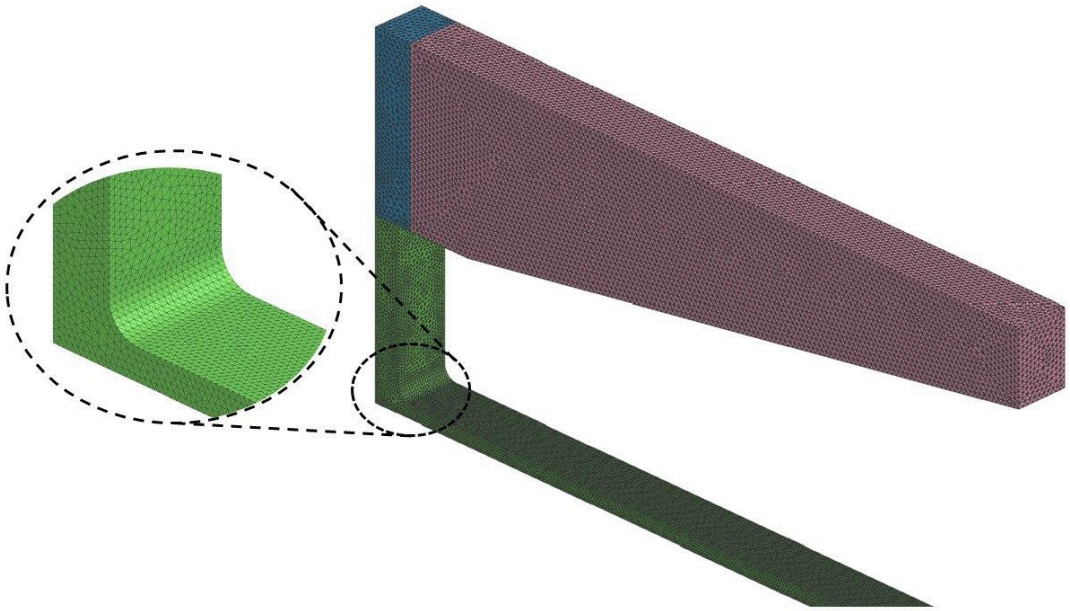

Figure 11 – 3D Geometry of the part and generated mesh

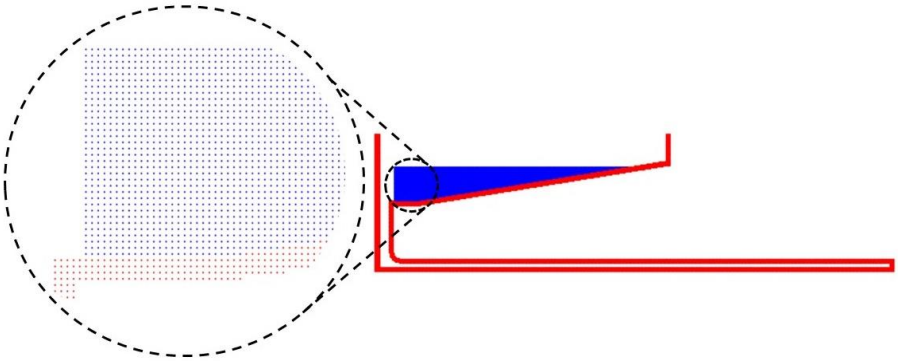

Figure 12 - SPH geometry schematic with 1mm distance between particles: blue (molten metal), red (mold)

4. Results and discussion

4.1 Study of filling stage

The metal filling time at various positions in the part is shown in Figure (13) for experimental data, SPH, and ProCAST simulation. It should be mentioned that the time between filling N1 (top of sprue) and N2 (bottom of sprue) has been removed from the total filling time, and N2 is regarded as a reference point in Figure (13).

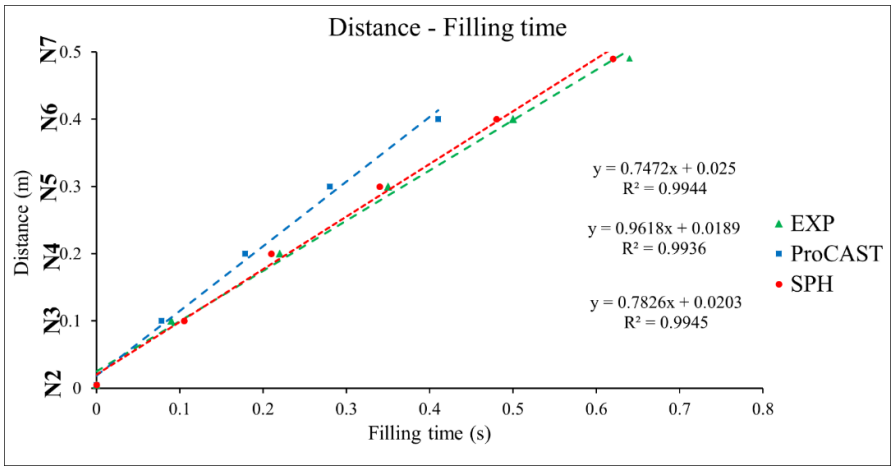

Figure 13 - Length of plate versus filling time for Experiment, ProCAST simulation, and SPH method

Figure (13) shows that for all three techniques, the correlation between distance and time is linear, resulting in a constant velocity value. The discrepancy between the experimental velocity (0.7472 m/s) and the velocity of ProCAST (0.9618 m/s) and SPH simulations (0.7826 m/s) is 25.1% and 4.63%, respectively.

N2 is 5mm distant from the start of the plate. The experimental analysis reveals that it takes 0.09s to go from N2 (5mm) to N3 (100mm), SPH approach overestimates it (0.105s), and the simulation using ProCAST underestimates it (0.078s). The experiment and SPH are increasingly consistent with each other as we go from N3 (100mm) to N4 (200m), and the SPH approach is able to replicate filling time (between N3 and N4) by 4.76% error. ProCAST and experimental filling time at N4 have a discrepancy of 25%. The gap between ProCAST and experimental data increases considerably by passing the N4 (200m) and reaching the N5 (300m), reaching 29.6% at this point. The filling time, does match well in N5 between the SPH technique and experimental data, by a variation of 2.94 %. The difference in filling time between ProCAST and SPH is 20.95 % while advancing to the end of the plate at position N6, which is 400 mm from the start of the plate. The SPH approach and the experiments have a roughly 4% variation in filling time. The filling time for the SPH method at location N7, which is 10 mm from the plate's end, is around 0.62s, whereas it is 0.64s in experiments and 0.53s in the ProCAST simulation. The experimental data and the SPH approach differ by 3.125 % and 14.5 %, respectively.

Even though the SPH solution is significantly closer to the experiment, both simulations indicate some errors. The difference between the experimental and SPH simulations is never more than 5%, demonstrating that the SPH approach successfully predicted fluid flow. SPH results show a slight overprediction on filling time until N4, and a corresponding underprediction beyond that. The trend line of filling time using Pro-CAST software is much lower than the experimental results and the SPH technique. In a conclusion, the divergence between experimental and ProCAST simulation is larger than 15% in most positions. The SPH method is a Lagrangian method that can more accurately simulate the filling of gravity castings by using artificial viscosity to increase stability. To keep the particles from separating, the viscosity level is set higher. Using the ProCAST simulation and SPH methodologies, Figures (14 to 20) depict the temperature and velocity field of the filling step at 0.1s, 0.2s, 0.3s, 0.4s, 0.5s, 0.6s, and 0.74s.

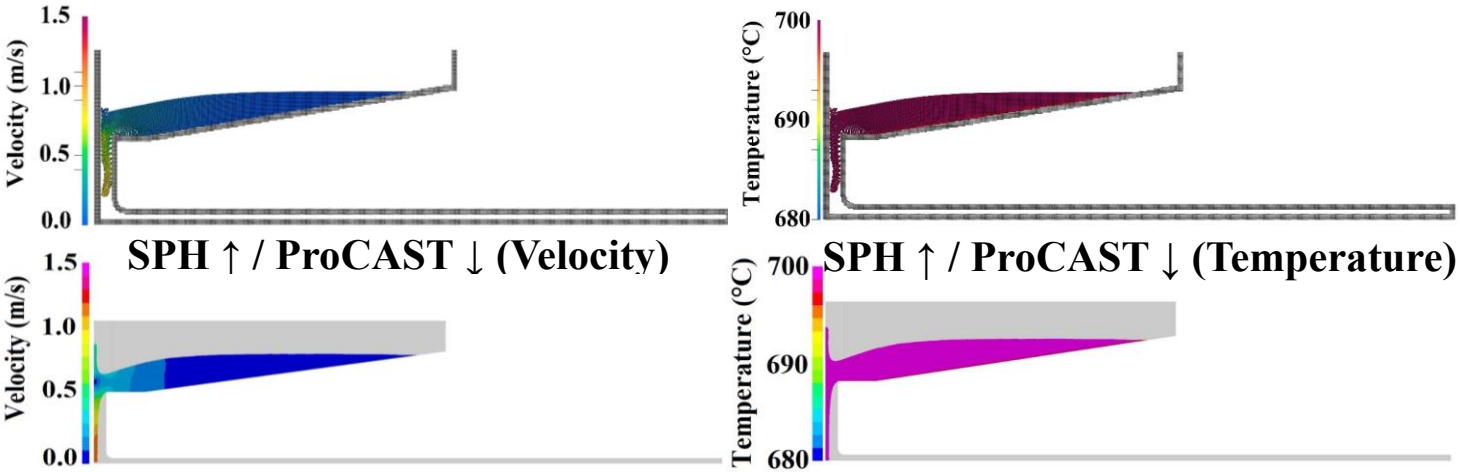

Figure 14 - Temperature and Velocity field during filling step of SPH and ProCAST simulation (0.1s)

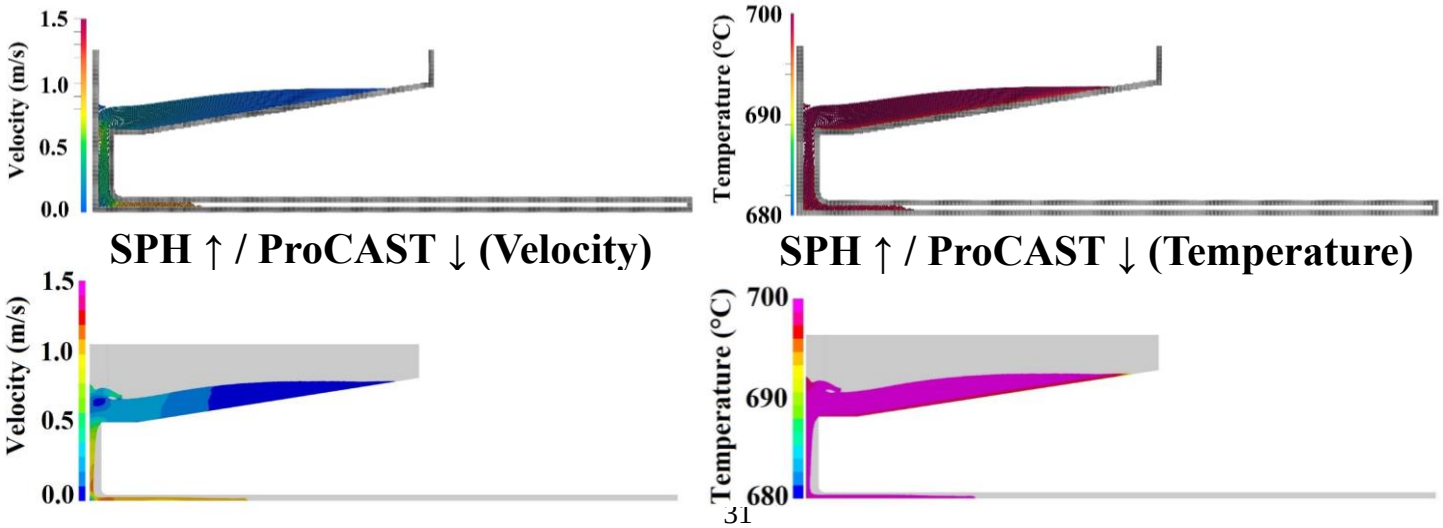

Figure 15 - Temperature and Velocity field during filling step of SPH and ProCAST simulation (0.2s)

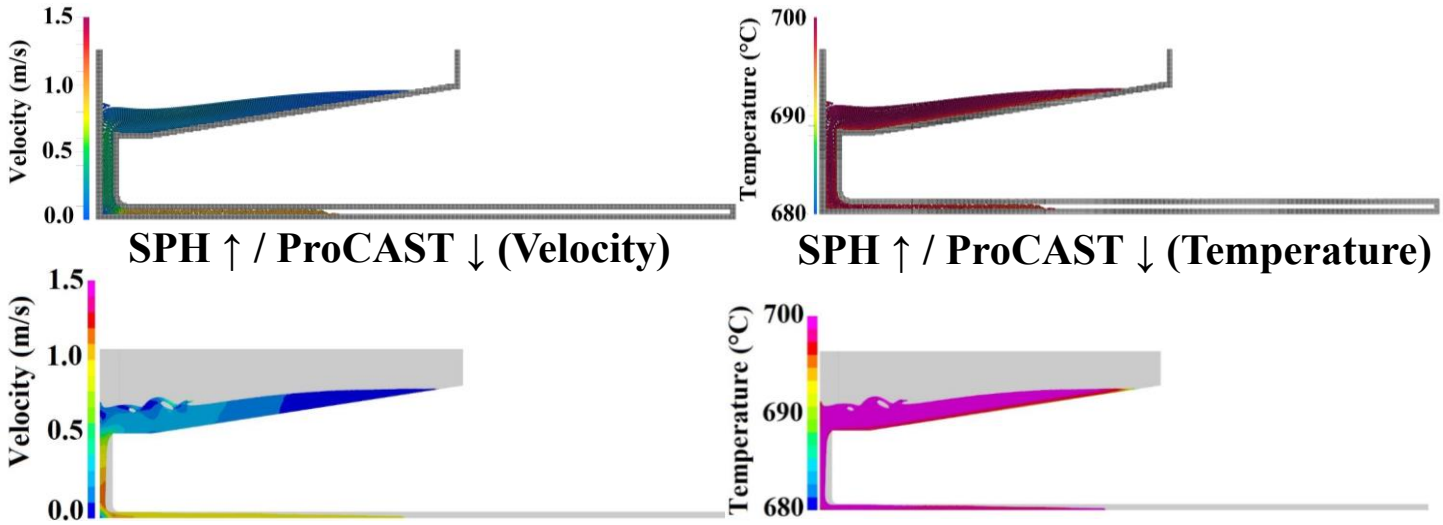

Figure 16 - Temperature and Velocity field during filling step of SPH and ProCAST simulation (0.3s)

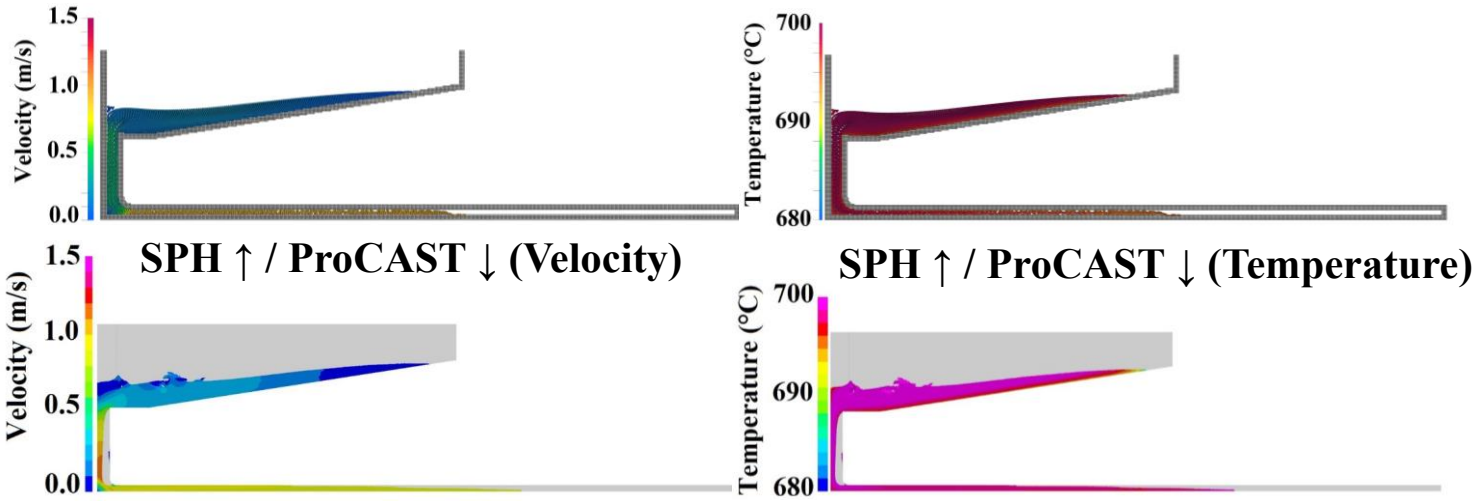

Figure 17 - Temperature and Velocity field during filling step of SPH and ProCAST simulation (0.4s)

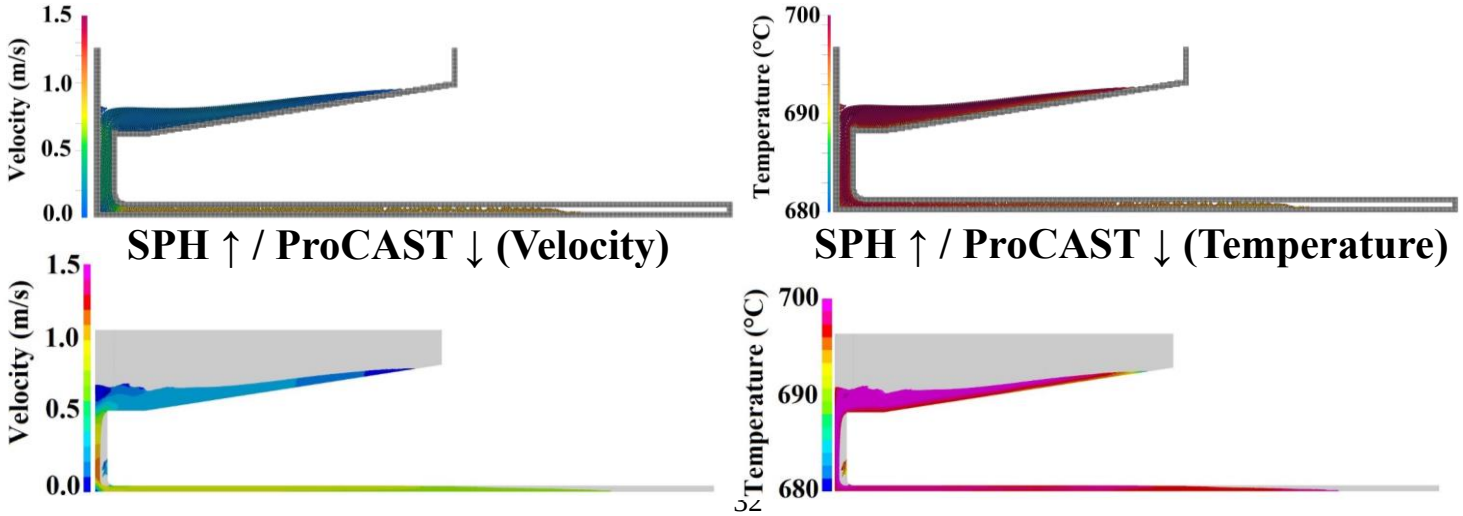

Figure 18 - Temperature and Velocity field during filling step of SPH and ProCAST simulation (0.5s)

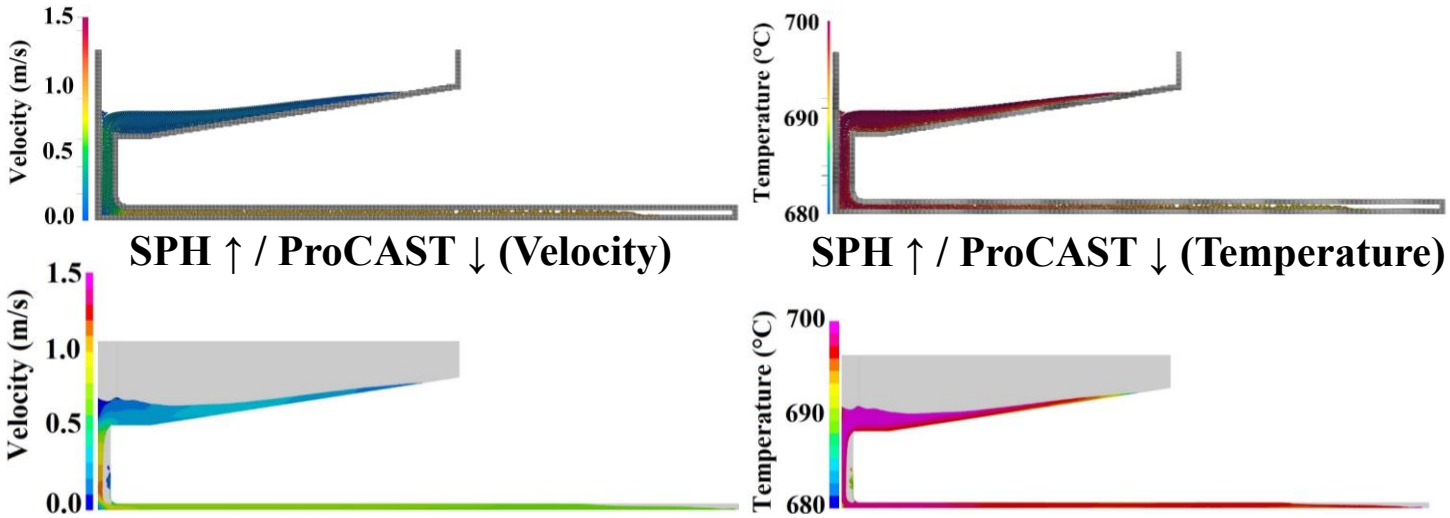

Figure 19 - Temperature and Velocity field during filling step of SPH and ProCAST simulation (0.6s)

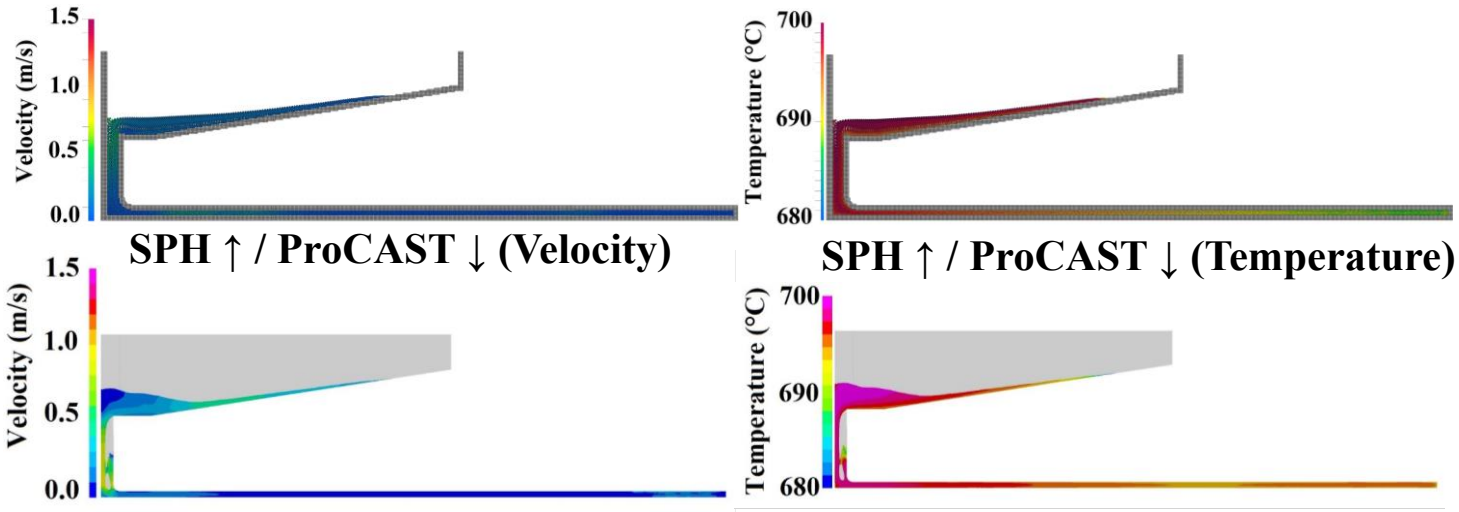

Figure 20 - Temperature and Velocity field during filling step of SPH and ProCAST simulation (0.74s)

is more than SPH at the beginning of filling (0.1s). In ProCAST simulation, the fluid going through the sprue sticks to one side and moves downward, having reached the bottom of the sprue after 0.1s. With SPH technique, on the other hand, approximately 2/3 of the sprue is filled by the maximum velocity of 0.9m/s. Regarding the temperature field, it should be underlined that the temperature in both simulations is 698°C at the end of 0.1s.

At (0.2s), the differences between ProCAST solution and the experiment get larger as shown in Figure (15), while the SPH solution compares more favorably based on comparison with experimental results. The fluid

has moved to a length of 100mm in the ProCAST approach, whereas it has advanced to a length of 75mm in SPH approach in 0.2s. A thin layer of molten material is flowing over the plate in the ProCAST process, approximately half the thickness of the plate, and as the flow continues, the thickness decreases. It is worth noting that half of the sprue in ProCAST is still empty at this point, while in the SPH method, it is entirely filled. The velocity of the molten metal is higher near the bottom of the plate than at the top of it in the SPH method due to gravity. This is assumed to be due to the simulation's absence of air. The temperature begins to reduce slowly after 0.2s, and variations in the molten metal are visible near the ramp's surface, with temperatures reaching 695°C in certain positions of SPH.

In the ProCAST technique, molten metal passe more than half the plate at time 0.3s, whereas in the SPH approach, it is still a long way from filling half the plate (Figure (16)). In the pouring basin and plate, temperature changes from the walls to the inside of the flow in 0.3s are clear for both numerical methodologies.

As demonstrated in Figure (17), half of the plate is filled in SPH method, whereas the filling process in ProCAST simulation approached 60% of the plate. Figure (17) indicates that temperature continues to drop in the plate when the temperature in the SPH technique approaches 692°C, whereas the minimum temperature in ProCAST approach remains 695°C along the plate.

Figure (18) shows that in SPH approach and ProCAST simulation at 0.5s, filling reaches over 65% and 75%, respectively. At 0.5s, advancing from the bottom of the sprue to the end of the plate using the SPH technique, it is clear that the temperature progressively decreases from 697°C to 690°C as we go closer to the end of the plate. Regardless of the fact that this pattern is less visible, the temperature gradient in the middle and even in front of flow utilizing the ProCAST approach is still 700°C.

The filling stage is practically complete in frame 0.6s and ends in time 0.62s, as seen in Figure (19). The SPH method fills 80 percent of the plate after 0.6 seconds.

To sum up, Figure (20) presents the state of filling using ProCAST and SPH at 0.74s. The period from the start of the filling to the completion of the filling corresponds to 0.62s in ProCAST method and 0.74s in the SPH corresponding to 19.3% gap. The highest velocity in the filling stage of the SPH approach is roughly 0.9m/s, while it is around 1.1m/s for ProCAST. It should be noticed that the SPH method's filling temperature balance is more homogeneous in 0.74s than ProCAST. The temperature in some areas of the plate is lower than the end of plate at the end of filling step in ProCAST simulation. The SPH shows sustainable agreement with the experiment at all late stages of the filling process, with accurate estimates of the speed of fluid front propagation and filling times. The ProCAST simulation, on the other hand, quickly diverges from the experimental flow, with considerable inaccuracies anticipated in the filling time estimate.

4.2 Study of solidification step

The cooling curves for points N3, N4, N5, and N6 as well as cooling rate and solidification time for three zones are presented in Figure (21) and Table (5), respectively. Since the thermal properties of the sand and the alloy were not experimentally described, the comparison between experimental and numerical results is qualitative.

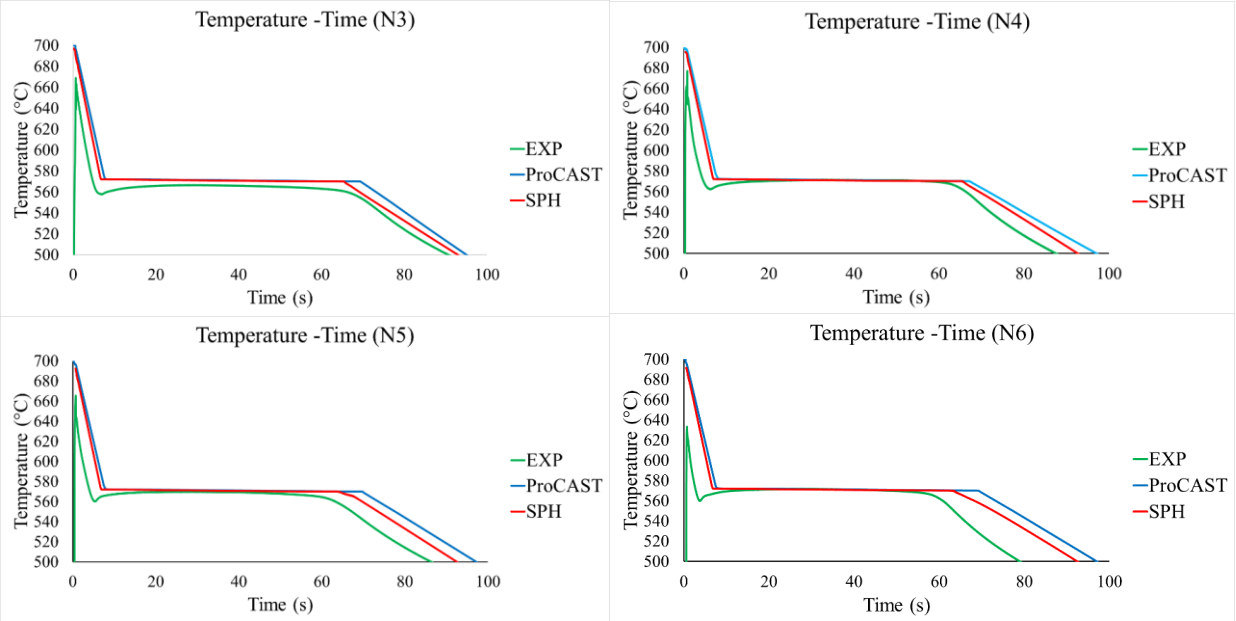

Figure 21 - Temperature evolution of point N3, N4, N5 and N6

Table 5 - Comparison of temperature drop rates $\left(\frac{C^{\circ}}{s}\right)$ in liquid (zone 1) and solid (zone 3) and solidification time (s) (zone 2) for N3, N4, N5 and N6 using experimental data, SPH and ProCAST

Methods/Points	N3			N4			N5			N6		
Zone	**1**	**2**	**3**	**1**	**2**	**3**	**1**	**2**	**3**	**1**	**2**	**3**
Experiment	**20.37**	**60.83**	**2.29**	**21.08**	**57.5**	**2.52**	**23.84**	**57**	**2.32**	**21.30**	**57**	**2.73**
SPH	**19.44**	**59.32**	**2.12**	**18.65**	**58.18**	**2.57**	**19.05**	**56.54**	**2.45**	**19.02**	**56.1**	**2.43**
ProCAST	**15.61**	**60.64**	**2.18**	**15.01**	**58.51**	**2.34**	**14.7**	**60.75**	**2.55**	**15.38**	**60.37**	**2.51**

Table (5) compares four measures at positions N3 to N6, the average cooling rate between maximum temperature and liquidus temperature (zone 1), the cooling rate at solid state (zone 3), and solidification time (zone 2). Cooling rates are given in degrees Celsius per second $(\frac{C^{\circ}}{s})$ in zone 1 and 3, and solidification time for zone 2 in seconds.

N3: The results of Point N3, as shown in Table (5) and Figure (21), indicate that the values of cooling rate between experiment $(20.37\frac{C^{\circ}}{s})$ and SPH $(19.44\frac{C^{\circ}}{s})$ are consistent whereas there is a significant difference with the cooling curve of ProCAST $(15.61\frac{C^{\circ}}{s})$. The solidification time between experiment and ProCAST, as well as between experiment and SPH, is consistent with a difference of 0.31% and 2.48%, respectively, according to the data in Table (5). ProCAST's rate of temperature $(2.18\frac{C^{\circ}}{s})$ decline in the solid zone of N3 is closer to experiment than $(2.29\frac{C^{\circ}}{s})$ the SPH technique $(2.12\frac{C^{\circ}}{s})$ but cooling is underestimated in both simulations.

N4: Figure (21) also shows the temperature evolution for N4 using experimental and numerical data. The rate of temperature drop for experimental data at liquid and solid states is larger compared to N3, whereas numerical simulations SPH and ProCAST have reduced at point N4 in the first zone. In first zone, the experimental data with SPH and ProCAST differ by 11.53% and 28.8%, respectively, due to this issue. By moving forward the boundary conditions at the end of the plate, the solidification time in all three methods

has been slightly reduced in the second zone. The disparity between the solidification time of experimental data and numerical findings is less than 2%. The rate of cooling in the solid state of SPH for N4 is more valid than the ProCAST simulation. It should be noted that SPH overestimates solidification time, whereas ProCAST underestimates.

N5: In the first zone of N5 which is shown in Figure (21), the rate of temperature decrease is still higher in experimental data than in both numerical simulations. It should be noted that the SPH method is still much closer to the experimental data than ProCAST simulation. For experiment and SPH, solidification time decrease with a low slope, however, this value grows in ProCAST. In the third area, both numerical techniques underestimate the rate of temperature drop, with SPH being closer to experimental data.

N6: The rate of temperature drop in the experimental data remains higher than the simulation at point N6 in Figure (21); the difference between the experiments and SPH is 10.70 %. In addition, the gap between the experiments and ProCAST is 27.80%. It should be emphasized that experimental data and SPH show the shortest solidification time at this point. When compared to SPH, the ProCAST approach is more consistent with experimental data in the solid state of N6.

To summarize, the cooling rate for all positions in the first zone is greater for the experiment, while the SPH approach is significantly capable of predicting such temperature reduction rate with a global maximal error of 11.73%. The gap between experiential data and ProCAST is higher, ranging between 24% and 39%. In the solidification zone, the solidification time should decrease as one gets closer to the end of the plate, which is observed and well predicted in experimental data and the SPH technique, unlike ProCAST.

It should also be highlighted that the highest difference between the maximum and minimum solidification time is 6.3 %, 5.4 %, and 3.7 % for experiment, SPH, and ProCAST. This clearly demonstrates that the boundary condition at the end of the plate has little impact on solidification time. The most substantial variation among experimental data and SPH is 11% and experimental data and ProCAST is 9%. It should be mentioned that in the third zone, the solid cooling rate value ranges from $(2.12\frac{C^{\circ}}{s})$ to $(2.73\frac{C^{\circ}}{s})$ for all

four points and all approaches. Additionally, SPH technique predicted more accurately at points N4 and N5, and ProCAST approach performed better at points N3 and N6. It is therefore impossible to determine with certainty whether method models better cooling in zone 3. In the whole zone 1 and 2, SPH is able to predict the trend of temperature evolution better than ProCAST. The results demonstrate that the two numerical approaches differ in the filling time and cooling during the filling stage as well as the cooling and solidification times during the solidification stage of the gravity casting process. The variations between the results of these two numerical modelings can be attributed to two important factors. Firstly, it could well result from fundamentally different methods, especially during filling. ProCAST uses the Eulerian approach (Finite Element Method), while SPH uses the Lagrangian approach. It should be noted that the Navier-Stokes equation's pressure gradient and diffusion term are derived in different ways using the two different numerical approaches, which could lead to discrepancies during the filling of gravity castings. Moreover, continuity and momentum contain mathematical operators like gradient, divergence, and Laplace and the discretization methods used in FEM and SPH are different, the results may vary. Secondly, different definitions of thermophysical parameters lead to a rise in the difference between SPH and Pro-CAST in terms of cooling and solidification. In contrast to SPH simulation, which employs equation (17) utilizing QuikCAST database to establish heat capacity and density, Pro-CAST simulation used pre-defined databases. Additionally, latent heat is added as an equivalent heat capacity to the solidification term in the energy equation of SPH, whereas it is added as a source term in ProCAST.

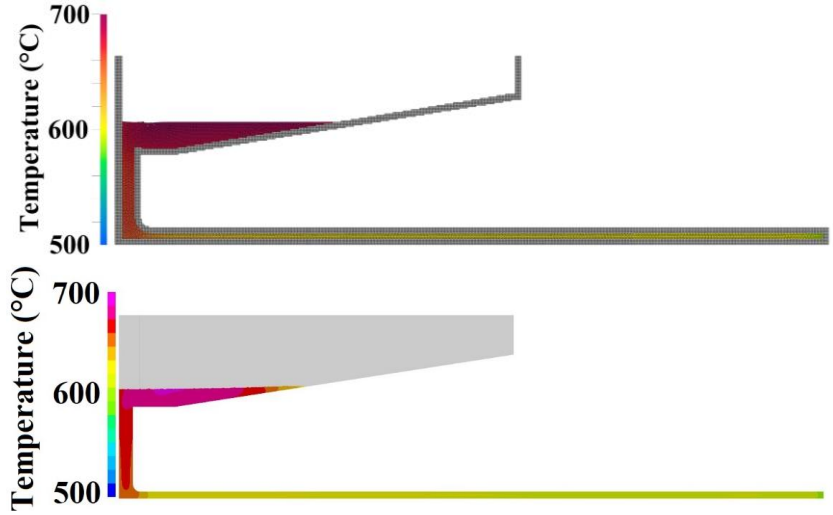

Figure 22 - Temperature field during cooling of simulation using SPH (top) and ProCAST (bottom) at 5s

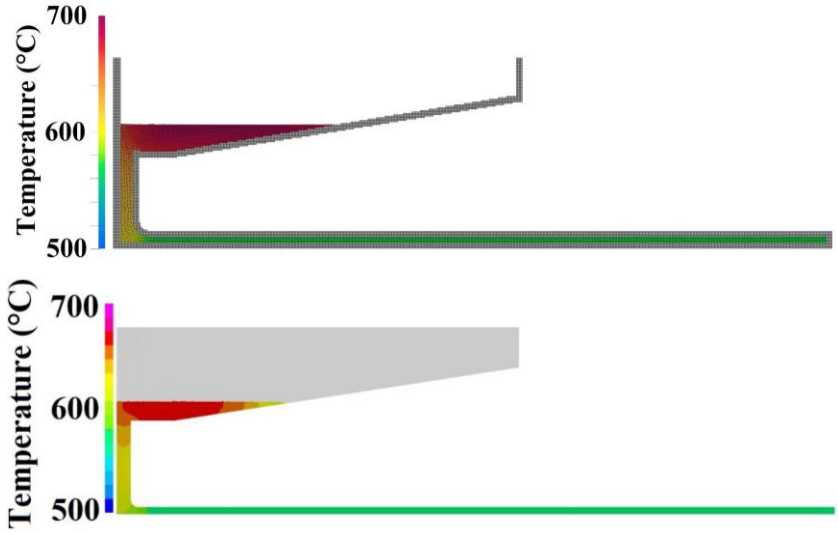

Figure 25 - Temperature field during cooling of simulation using SPH (top) and ProCAST (bottom) at 10s

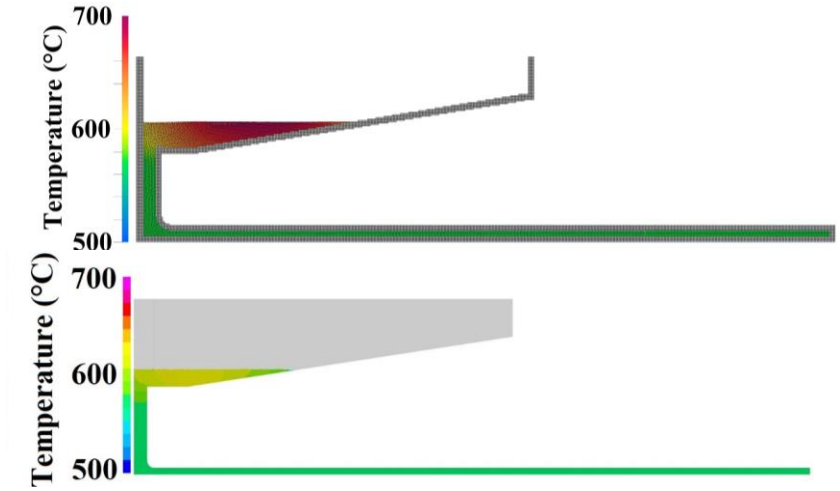

Figure 24 - Temperature field during solidification of simulation using SPH (top) and ProCAST (bottom) at 30s

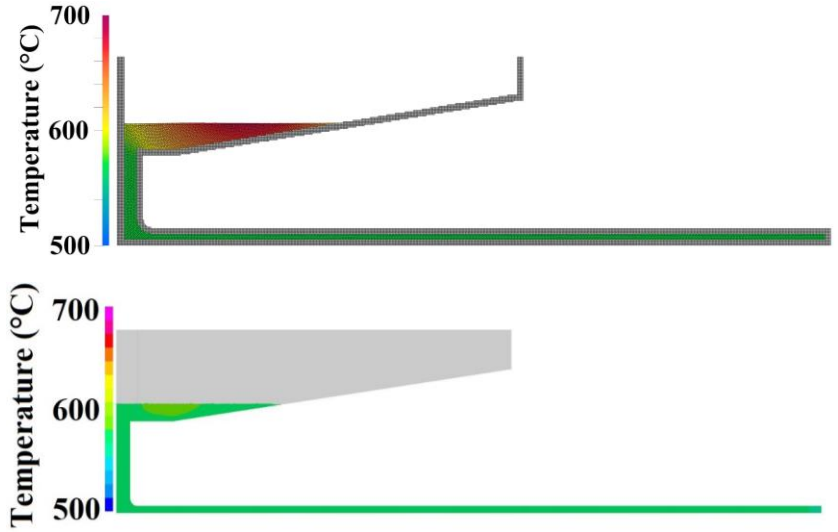

Figure 23 - Temperature field during solidification of simulation using SPH (top) and ProCAST (bottom) at 50s

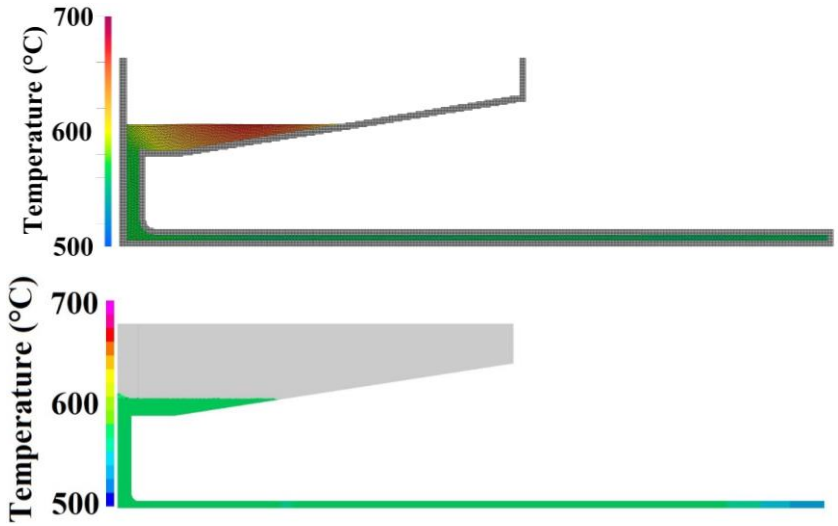

Figure 26 - Temperature field during solidification of simulation using SPH (top) and ProCAST (bottom) at 70s

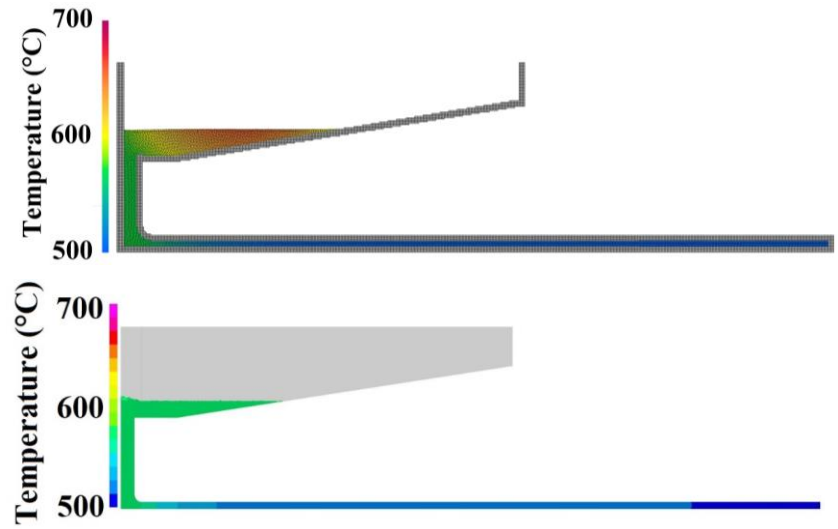

Figure 27 - Temperature field during solidification of simulation using SPH (top) and ProCAST (bottom) at 90s

Figure (22) shows the temperature change trend after 5s. The temperature of the plate starts out around 640°C degrees and goes to 590°C in both techniques. In both methodologies, the temperature field follows the same pattern of temperature change over time and plate length. The solidification process for both simulations begins after 10s and the temperature on the plate is lower than 572°C in the whole plate and about 620°C in the sprue. A significant part of the sprue is solidifying after 30s (Figure (24)), and the process of phase transition and temperature decrease on the plate. The solidification process at the end of the plate is complete for both ways by the time it reaches 50s, as shown in Figure (25), and it propagates across the entire plate. At 70s, Figure (26) displays the temperature field. The solidification process is complete for

the entire plate, as indicated in the previous Tables and Figures. The temperature in a major part of the plate in both simulations is between 550°C and 500 °C after 90s, as illustrated in Figure (27). It is worth noting that as we move further to the plate's end, the temperature drops around 100°C.

5. Conclusion

This article presents a study that aims to design a universal test case for a closed system that could be simulated in 2D to analyze velocity and temperature fields during the processes of filling, cooling, and solidification. The design of the universal test case considers the width as unimportant in comparison to the length and thickness when it comes to filling and cooling. Developing a universal test case of a closed system capable of replicating the two-dimensional filling, cooling, and solidification phases of the casting process is an interesting aspect of the development of numerical approaches. Specifically, the study compares the Smoothed Particle Hydrodynamics (SPH) technique with the ProCAST commercial software in modeling the 2D filling and solidification of gravity casting. Experimental results of gravity casting of AlSi13 using a 3D printed mold are compared to numerical data obtained from SPH and ProCAST software in terms of filling and solidification.

The key finding of this investigation is that the SPH approach, when utilizing artificial viscosity modeling, is able to accurately replicate casting filling. Thermal results indicate that both methods, using Neumann thermal boundary conditions derived from experimental data, successfully reproduce the cooling and solidification of the gravity casting process. Comparisons between the numerical and experimental results demonstrate that the SPH approach outperforms ProCAST in simulating cooling and solidification. This superiority is attributed to the fundamental methodology and thermophysical properties of the SPH approach. SPH exhibits better accuracy in modeling

the rate of heat dissipation in the liquid state and the trend of solidification time along the plate's length.

In conclusion, the introduction of a universal test case for gravity casting of closed systems enables the modeling of filling and solidification in two dimensions and facilitates the validation of numerical simulations such as the SPH approach and ProCAST.

Acknowledgements The authors acknowledge the contribution of colleagues. Thanks are due to J. Bourgeois and J. Nègre of the Arts et Metiers ParisTech for their technical support.

Author contribution Mohammad Zarbini Seydani: Numerical simulation, Investigation, data curation, Methodology, Writing-Original draft.

Abdelkader Krimi: Numerical simulation, Methodology, Conceptualization.

Marie Bedel: Experimental work, Investigation, Methodology, Conceptualization.

Sofiane Khelladi: Numerical simulation, Methodology, Conceptualization.

Mohamed El Mansori: Supervision, Conceptualization, Methodology.

Availability of data and material The data supporting the conclusion of this article are included within the article. Any queries regarding these data may be directed to the corresponding author

Declarations

Ethical approval Not applicable.

Consent to participate All the authors agree to participate in this research study.

Consent to publish The authors consent to have the data published.

Competing interests The authors declare no competing interests.

Funding: Institut Carnot ARTS

6. References

[1] F. Bonollo, J. Urban, B. Bonatto, M. Botter, "Gravity and low pressure die casting of aluminium alloys: a technical and economical benchmark," *La Metallurgia Italiana,* 2005.

[2] Guofa MI, Hengtao ZHAO, Kuangfei WANG, Zhian XU, Jitai NIU, "Simulation of Mold Filling and Solidification on Gravity Casting of Al-Si Alloy (A357)," *Materials Science Forum,* Vols. 575-578, pp. 1204-1209, 2008.

[3] B.Sorte.Madhukar, "Defects, Root Causes in Casting Process and Their Remedies: Review," *Journal of Engineering Research and Application,* vol. 7, no. 3, pp. 47-54, 2017.

[4] Abhilash Viswanath, M.V. Manu, S. Savithric, U.T.S. Pillai, "Numerical simulation and experimental validation of free surface flows during low pressure casting process," *Journal of Materials Processing Technology,* vol. 244, pp. 320-330, 2017.

[5] J. Jakumeit, E. Subasic, M. Bu¨nck, "Shape Casting: 5th International Symposium," (Wiley, San Diego), 2014.

[6] B. Zhang, S.L. Cockcroft, D.M. Maijer, J.D. Zhu, and A.B. Phillion, "Casting Defects in Low-Pressure Die-Cast Aluminum Alloy Wheels," *JOM,* 2005.

[7] P. D. Ingle, B. E. Narkhede, "A Literature Survey Of Methods To Study And Analyze The Gating System Design For Its Effect On Casting Quality," *Materials Today: Proceedings,* vol. 5, pp. 5421-5429, 2018.

[8] K Ellingsen, T Coudert, and M M'Hamdi, "SPH based modelling of oxide and oxide film formation in gravity die castings," *IOP Conf. Ser.: Mater. Sci. Eng.*, vol. 84, 2015.

[9] Mahesh Prakasha, Paul Cleary, John Grandfield, "Modelling of metal flow and oxidation during furnace emptying using smoothed particle hydrodynamics," *journal of materials processing technology,* vol. 209, p. 3396–3407, 2009.

[10] B. Minaie, K. A. Stelson, V. R. Voller, "Analysis of Flow Patterns and Solidification Phenomena in the Die Casting Process," *journal of engineering materials and technology,* vol. 113, pp. 296-302, 1991.

[11] Shan-guang Liu, Chuan-biao Luo, Guo-ai Li, Wen-lin Gao, Zheng Lu, Sheng-long Dai, "Effect of pressurizing speed on filling behavior of gradual expansion structure in low pressure casting of ZL205A alloy," *Research & Development,* vol. 15, no. 4, p. 276–282, 2018.

[12] Ik-Tae Im, Woo-Seung Kim, Kwan-Soo Lee, "A Unified analysis of filling and solidification in casting with natural convection," *International Journal of Heat and Mass Transfer,* vol. 44, pp. 1507-1515, 2001.

[13] G. Kreziak, C. Rigaut, and M. Santarini, "Low pressure permanent mould process simulation of a thin wall aluminum casting," *Materials Science and Engineering,* pp. 255-259, 1993.

[14] Zitian, Jiang Wenming and Fan, "Gating system optimization of low pressure casting A356 aluminum alloy intake manifold based on numerical simulation," *Research & Development CHINA FOUNDRY,* vol. 11, no. 2, 2014.

[15] Mi Guofa, Liu Xiangyu, Wang Kuangfei, Fu Hengzhi, "Numerical simulation of low pressure die-casting aluminum wheel," *China foundary,* vol. 6, 2008.

[16] Joseph Ha, Paul Cleary, Vladimir Alguine and Thang Nguyen, "Simulation of die filling in gravity die casting using sph and magmasoft," in *Second International Conference on CFD in the Minerals and Process Industries*, CSIRO, Melbourne, Australia, 1999.

[17] Ting Ye, Dingyi Pan, Can Huang, and Moubin Liu, "Smoothed particle hydrodynamics (SPH) for complex fluid flows: Recent developments in methodology and applications," *Physics of Fluids,* vol. 31, no. 1, 2018.

[18] M. Y. Hu, J. J. Cai, N. Li, H. L. Yu, Y. Zhang, B. Sun, and W. L. Sun, "Flow modeling in high-pressure die-casting processes using sph model," *International Journal of Metalcasting,* vol. 12, p. 97–105, 2018.

[19] Xiaofeng Niu, Jingyu Zhao, Baojian Wang, "Application of smooth particle hydrodynamics (SPH) method in gravity casting shrinkage cavity prediction," *Computational Particle Mechanics,* vol. 6, pp. 803-810, 2019.

[20] P.Cleary, J. Ha, M.Sawley, "Modelling industrial fluid flow application using SPH," in *Proceedings of the International Workshop on Bifurcation and Localisation*, 1999.

[21] Wen-jiong CAO, Zhao-yao ZHOU, Fang-ming JIANG, "Smoothed particle hydrodynamics modeling and simulation of foundry filling process," *Trans. Nonferrous Met. Soc. China,* vol. 25, pp. 2321-2330, 2015.

[22] U. CHANDRA, "Benchmark problems and testing of a finite element code for solidification in investment castings," *INTERNATIONAL JOURNAL FOR NUMERICAL METHODS IN ENGINEERING,* vol. 30, pp. 1301-1320, 1990.

[23] B. Sirrell, M. Holliday, and J. Campbell, "Benchmark Testing the Flow and Solidification Modeling of AI Castings," *JOM,* vol. 48, pp. 20-23, 1996.

[24] F. Bonollo, J. Urban, B. Bonatto, M. Botter, "Gravity and low pressure die casting of aluminium alloys: a technical and economical benchmark," *la metallurgia italiana,* no. 6, 2005.

[25] Tommy carozzani, Charles-andre´gandin, Hugues digonnet, Michel bellet, Kader zaidat, and Yves fautrelle, "Direct Simulation of a Solidification Benchmark Experiment," *Metallurgical and materials transactions a,* vol. 44A, 2013.

[26] Ondrej Bublık, Libor Lobovsky, Vaclav Heidler, Tomas Mandys and Jan Vimmr, "Experimental validation of numerical simulation of free-surface flow within casting mold cavities," *Engineering Computations,* vol. 38, pp. 4024-4046, 2021.

[27] Nicolas Coniglio, Tharmalingam Sivarupan, Mohamed El Mansori, "Investigation of process parameter effect on anisotropic properties of 3D printed sand molds," *The International Journal of Advanced Manufacturing Technology,* vol. 94, p. 2175–2185, 2018.

[28] M. Zamani, "Al-Si Cast Alloys -Microstructure and Mechanical Properties at Ambient and Elevated Temperature," Jönköping University, School of Engineering, Dissertation, 2017.

[29] Mariem Ben Saada, Mohamed El Mansori, "Assessment of the effect of 3D printed sand mold thickness on solidification process of AlSi13 casting alloy," *The International Journal of Advanced Manufacturing Technology,* vol. 114, pp. 1753-1766, 2021.

[30] C.Prakash and V. R.Voller, "A fixed grid numerical modelling methodology for convection-diffusion mushy region phase-change problems," *International Journal of Heat and Mass Transfer,* vol. 30, no. 8, p. 1709–1719, 1987.

[31] J.J.Monaghan, "simulating free surface flows with sph," *Journal of computational physics,* vol. 110, no. 2, pp. 399-406, 1994.

[32] Abdelkader Krimi, Mehdi Rezoug, Sofiane Khelladi, Xesús Nogueira, Michael Deligant, Luis Ramírez, "Smoothed Particle Hydrodynamics: A consistent model for interfacial multiphase fluid flow simulations," *Journal of Computational Physics,* vol. 358, pp. 53-87, 2018.

[33] M.B. Liu and G.R.Liu, "Smoothed Particle Hydrodynamics (SPH): an Overview and recent developments," *Arch Comput Methods Eng,* vol. 17, pp. 25-76, 2010.

[34] Paul W. Cleary, Joseph Ha, Mark L. Sawley, "Modelling Industrial Fluid Flow Applications using SPH," in *Bifurcation and Localisation Theory in Geomechanics*, CRC Press, 2001, p. 8.

[35] P.W. Cleary, J. Ha, M. Prakash, T. Nguyen, "3D SPH flow predictions and validation for high pressure die casting of automotive components," *Applied Mathematical Modelling,* vol. 30, pp. 1406-1427, 2006.

[36] Liu M.B. Liu G.R., "Smoothed Particle Hydrodynamics (SPH): an Overview and Recent Developments," *Arch Comput Methods Eng,* vol. 17, pp. 25-67, 2010.

[37] P.N. Sun, A. Colagrossi, S. Marrone, A.M. Zhanga, "The δplus-SPH model: Simple procedures for a further improvement of the SPH scheme," *Comput. Methods Appl. Mech. Engrg.,* vol. 315, p. 25–49, 2017.

[38] M. Antuono, A. Colagrossi, S. Marrone, "Numerical diffusive terms in weakly-compressible SPH schemes," *Comput. Phys. Comm.,* vol. 183, pp. 2570-2580, 2012.

[39] Domenico D. Meringolo, Salvatore Marrone, Andrea Colagrossi, Yong Liua, "A dynamic δ-SPH model: How to get rid of diffusive parameter tuning," *Computers and Fluids,* vol. 179, p. 334–355, 2019.

[40] Domenico D. Meringolo, Yong Liu, Xin-Yu Wang, Andrea Colagrossi, "Energy balance during generation, propagation and absorption of gravity waves through the δ-LES-SPH model," *Coastal Engineering,* vol. 140, p. 355–370, 2018.

[41] Domenico D. Meringolo, Salvatore Marrone, Andrea Colagrossi, Yong Liua, "A dynamic δ-SPH model: How to get rid of diffusive parameter tuning," *Computers and Fluids,* vol. 179, p. 334–355, 2019.

[42] Domenico D. Meringolo, Yong Liu, Xin-Yu Wang, Andrea Colagrossi, "Energy balance during generation, propagation and absorption of gravity waves through the δ-LES-SPH model," *Coastal Engineering,* vol. 140, p. 355–370, 2018.

[43] M. Antuonoa, A. Colagrossi ,S. Marronea, "Numerical diffusive terms in weakly-compressible SPH schemes," *Computer Physics Communications,* vol. 183, p. 2570–2580, 2012.

[44] J.J. Monaghan, R. A. Gingold, "Shock Simulation by the Particle Method SPH," *journal of computational physics,* vol. 52, pp. 374-389, 1983.

[45] A. Brent, V. Voller, and K. Reid, "Enthalpy-porosity technique for modeling convection-diffusion phase change: application to the melting of a pure metal," *Numerical Heat Transfer, Part A Applications,* vol. 13, no. 3, p. 297–318, 1988.

[46] J. A. Mackenzie and M. L. Robertson, "The Numerical Solution of One-Dimensional Phase Change Problems Using an Adaptive Moving Mesh Method," *Journal of Computational Physics,* vol. 161, p. 537–557, 2000.

[47] Huespe, Víctor D. Fachinotti Alberto Cardona Alfredo E., "A Fast Convergent and Accurate Temperature Model for Phase-change Heat Conduction," *Int. J. Numer. Meth. Engng.,* vol. 44, pp. 1863-1884, 1999.

[48] J. Crank, "Free and moving boundary problems, " 1984.

[49] G.H.Meyer, "Multidimensional stefan problems," *SIAM Journal on Numerical Analysis,* vol. 10, no. 3, p. 522–538, 1973.

[50] P. W. Egolf and H.Manz, "Theory and modeling of phase change materials with and without mushy regions," *International Journal of Heat and Mass Transfer,* vol. 37, no. 18, p. 2917–2924, 1994.

[51] Schwaiger, Hans F., "An implicit corrected SPH formulation for thermal diffusion with linear free surface boundary conditions," *INTERNATIONAL JOURNAL FOR NUMERICAL METHODS IN ENGINEERING,* pp. 647-671, 2008.

[52] S. Adami, X. Hu, and N. Adams, "A generalized wall boundary condition for smoothed particle hydrodynamics," *Journal of Computational physics,* vol. 231, no. 21, pp. 7057-7075, 2012.

[53] Peng Lan, Jiaquan Zhang, "Study on the mechanical behaviors of grey iron mould by simulation and," *Materials and Design,* vol. 53, pp. 822-829, 2014.

[54] Su-Ling Lu, Fu-Ren Xiao, Shuang-Jie Zhang, Yong-Wei Mao, Bo Liao, "Simulation study on the centrifugal casting wet-type cylinder liner based on ProCAST," *Applied Thermal Engineering,* vol. 73, pp. 512-521, 2014.

[55] Hua. Wu, Haiming. Shi, Haifeng. Liu, Zhenjia.Xia, "Numerical Simulation of Flow Field and Temperature Field on Aluminium Alloy Engine Cylinder in Casting Process," *Materials Science Forum,* Vols. 704-705, pp. 50-57, 2012.